



United States Department of Commerce  
Technology Administration  
National Institute of Standards and Technology

*NISTIR 3992*

**STRUCTURE-PROPERTY RELATIONSHIPS IN  
MICROALLOYED FERRITE-PEARLITE STEELS  
PHASE 1: LITERATURE REVIEW, RESEARCH  
PLAN, AND INITIAL RESULTS**

---

---

P.T. Purtscher  
Yi-Wen Cheng

~~QC~~  
100  
.U56  
#3992  
1993



**NISTIR 3992**

# **STRUCTURE-PROPERTY RELATIONSHIPS IN MICROALLOYED FERRITE-PEARLITE STEELS PHASE 1: LITERATURE REVIEW, RESEARCH PLAN, AND INITIAL RESULTS**

---

---

P.T. Purtscher  
Yi-Wen Cheng

Materials Reliability Division  
Materials Science and Engineering Laboratory  
National Institute of Standards and Technology  
Boulder, Colorado 80303-3328

July 1993



---

U.S. DEPARTMENT OF COMMERCE, Ronald H. Brown, Secretary  
NATIONAL INSTITUTE OF STANDARDS AND TECHNOLOGY, Raymond G. Kammer, Acting Director



## CONTENTS

ABSTRACT	iii
1. INTRODUCTION	1
1.1 Economic Factors	1
1.2 Application History	3
1.3 Outlook for Future Applications	3
1.4 Current State of Understanding Strength-Toughness Relationships	4
1.4.1 Strength	4
1.4.1.1 Effect of Grain Size	7
1.4.1.2 Effect of Precipitation	7
1.4.1.3 Effect of Phase Transformation	10
1.4.1.4 Effect of Solid Solution Strengthening	13
1.4.1.5 Effect of Texture and Dislocations	13
1.4.1.6 Summary of Strength Effects	13
1.4.2 Hardness	15
1.4.3 Toughness	16
1.4.3.1 Impact Testing	16
1.4.3.2 Fracture Toughness Testing	19
1.4.3.3 Tensile Testing	21
1.4.3.4 Fatigue Testing	26
1.5 Summary	28
2. PROPOSED RESEARCH PROGRAM AT NIST	30
2.1 Generation of Representative Microstructures	31
2.2 Characterization of Structure	35
2.3 Determination of Properties	35
2.4 Integration of Structure and Properties for Modeling the Application	36

3.	PRELIMINARY STUDY	36
3.1	Introduction	36
3.2	Material and Experimental Procedures	36
3.3	Results	40
3.3.1	Microstructure	40
3.3.2	Mechanical Properties	40
3.3.3	Fractography	44
3.4	Discussion	46
3.5	Summary	51
4.0	ACKNOWLEDGEMENTS	52
5.0	REFERENCES	52
6.0	APPENDIX A -- Stress Analysis	58

## ABSTRACT

The literature related to the relationship between micro-structure and properties of steels after thermomechanical processing is reviewed and a plan for research is outlined. The goal is to provide a methodology which can predict the range of forging parameters that will produce acceptable properties in the as-forged condition. The first phase of the work will emphasize the micro-alloyed ferrite-pearlite steels used to replace quenched and tempered steels in forged automotive applications such as crankshafts and connecting rods. Emphasis is placed on predicting those properties which are related to service life as a function of process variables. In preliminary experiments on air-cooled, Nb-treated SAE 1141 steel, the tensile properties and ductile fracture behavior were not strong functions of the hot-deformation conditions. The condition with the finest ferrite grain size produced better impact properties. The tensile properties of the steel can be estimated from the microstructure, but the difference between predicted and measured values can be as great as 100 MPa.



## 1. INTRODUCTION

Additions of small amounts of microalloying (MA) elements to a basic C steel can produce properties in the air-cooled condition which rival those of more expensive steels which require extra processing (1-3). The most common MA elements are V, Nb, and Ti, but significant additions of Mn, S, Mo, and sometimes Si are also used along with the common MA elements to optimize the beneficial effect of MA. The following sections will cover background information on MA ferrite-pearlite ( $\alpha$ -P) steels.

### 1.1 Economic Factors

Ferrite-pearlite ( $\alpha$ -P) steels, like the free-machining, medium C grade SAE 1141, that have intentional additions of MA elements like Nb, V, and/or Ti can be used to replace quenched and tempered (Q&T) steels in applications where the steel is not subjected to severe impact loading. The replacement can result in a cost savings of approximately 30% (2). The cost advantages come in four areas: I. lower alloy content, II. elimination of heat treatment cycle, III. lower distortion, therefore no straightening or stress relief, and IV. better machinability.

Table 1 shows the composition for SAE 4140, a typical Q&T steel, and SAE 1141 steel, a typical MA  $\alpha$ -P steel. Q&T steels typically contain 1.5 to 3% alloy content (Cr, Ni, Mn, and Mo) in the composition so that the steel will have enough hardenability to form martensite throughout the section during heat treatment. MA  $\alpha$ -P steels typically contain a slightly higher Mn content (1.0 to 1.5%) than a Q&T steel (0.7 to 1.0%), but no intentional additions of Cr, Ni, and Mo. The other major difference in composition between 4140 and 1141 is the S content. With 0.080 to 0.100% S added to the MA steel, the machinability is enhanced compared to that of a typical Q&T steel containing 0.025% max. S content (1,3).

Table 1. Chemical composition of typical Q&T and  $\alpha$ -P steels (mass %).

steel	C	Mn	S	P	Cr	Ni	Mo	Si	MA
1141	0.42	1.49	0.099	0.015	0.06	0.06	0.01	0.26	0.04 Nb
4140	0.40	0.84	0.023	0.012	0.83	0.09	0.22	0.26	0.11 V

Figure 1 illustrates the different thermal cycles which are required for MA and Q&T steels. The properties of a MA steel like SAE 1141V are obtained by cooling the steel in air after processing. For a Q&T steel, the desired properties are only obtained after an extra heat treating cycle which follows processing. The

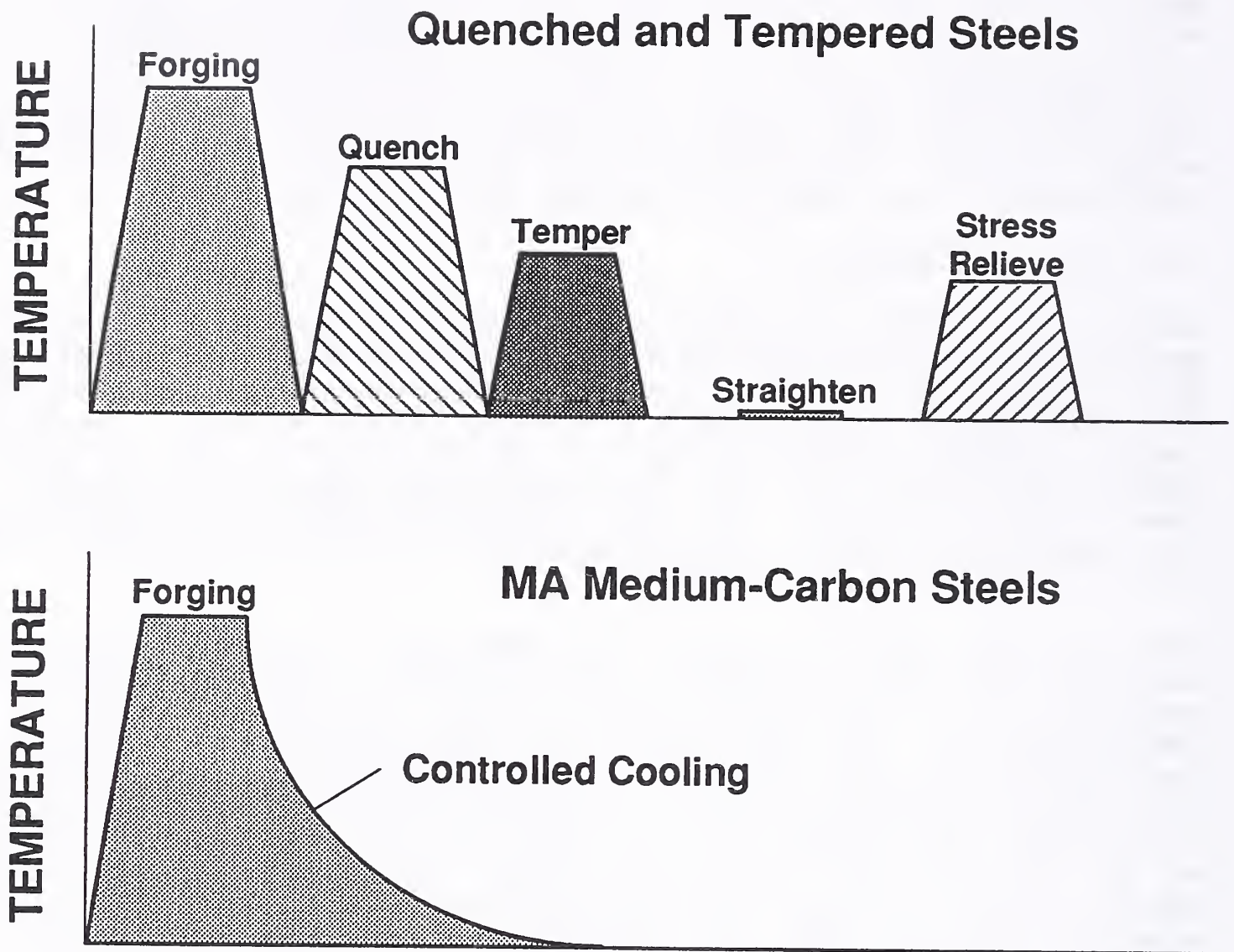


Fig. 1. Schematic diagram showing the advantages in manufacturing a crankshaft from MA  $\alpha$ -P steels rather than Q&T steels (1).

relatively slow cooling that the MA steel receives produces less distortion than the quench required for Q&T steels, and as a result, there are no additional costs due to straightening or stress relieving.

A recent study (4) has looked at a cost model for crankshaft processing. The paper examined the replacement of Q&T alloy and C steels (currently being used in production) with MA steel. The model considered fatigue and machinability data for the various steels. The MA steels offered a 10 to 20% reduction in cost, while at the same time providing equivalent fatigue and superior machinability characteristics.

## 1.2 Application History

MA forging steels were first used in Europe in the mid-1970's (5-7). With controlled cooling, the Europeans found that they could achieve a strength in  $\alpha$ -P steels with V added that was equivalent to typical Q&T steels. The reductions in processing and alloying costs were the initial incentive for replacing Q&T steels with MA  $\alpha$ -P steels, but later it became apparent that the machinability of precipitation strengthened  $\alpha$ -P steels was also superior to that of Q&T steels, which provided further cost advantages to the MA  $\alpha$ -P steels.

The application of these MA forging steels has been aggressively pursued since the late 1970's (7). The toughness of the MA forging steels was obviously lower than that of Q&T steels that had been historically used for forging. Therefore, comprehensive component testing programs were conducted by individual companies to form the basis for the substitution of MA steels for Q&T steels. The cumulative experience from component testing was positive; MA  $\alpha$ -P steels had adequate toughness for many applications like the connecting rod in a car engine and car steering knuckle. The lower toughness of the MA steels made it unacceptable for the front axle beam in a truck. Subsequent studies in the U.S.A. (8,9) have come to the same conclusion; MA  $\alpha$ -P steels have adequate toughness for many applications where Q&T steels have always been used.

A similar application for MA steels has been in the forging of track links for crawler-type tractors (10,11). In this case, the forging blanks are induction heated, forged, quenched directly from forging to room temperature, and then tempered to the desired hardness. The final microstructure is tempered martensite, but fewer processing steps are required compared to the traditional process where the steel is allowed to cool to room temperature after forging, reheated, and then Q&T. Here, the MA additions are for control of the grain size rather than for precipitation strengthening.

## 1.3 Outlook for Future Applications

MA  $\alpha$ -P steel can be used in any application where moderate strength, good fatigue resistance, and superior machinability are needed. Direct replacement of Q&T grades with MA  $\alpha$ -P steels dictates that the steel be processed with existing equipment and procedures while maintaining the strength of Q&T steels with an acceptable toughness. A significant problem is defining what is acceptable toughness. Q&T steels have been used in many applications where toughness did not limit the design. Typically, Charpy V-notch (CVN) impact testing has been used as the only measure of toughness, and the lower impact toughness of MA  $\alpha$ -P steel compared to Q&T steel has made wider application of the former difficult.

To improve the toughness properties of forging steels while maintaining similar strength levels, bainitic alloys have been developed with lower C content and higher Mn plus Mo for hardenability (12). The nominal designations are AISI 1522 and 1535. Higher MA additions are used to make up the strength that is lost by lowering the C content. The lower C content does limit the use of bainitic steels to applications that do not require surface induction hardening, like automotive underbody parts (13). Bainite, compared to  $\alpha$ -P, has a finer structure and is more uniform over the scale of a prior austenite grain.

Grassl et al. (14) have evaluated the properties of MA bainitic steels as compared to MA  $\alpha$ -P and Q&T steels. Initial results, Fig. 2, emphasize that Q&T steels have higher yield strength (YS) and absorbed energy in room temperature CVN testing than MA bainitic and  $\alpha$ -P steels. The temperature transition curves for CVN absorbed energy from the different steels are shown in Fig. 3 (15). Again, the Q&T steel (4140) appears much superior compared to the bainitic (0.24 and 0.35C-Mn-Mo-V) and  $\alpha$ -P (1045V) steels. The bainitic steels are comparable to Q&T steel only at relatively high temperatures ( $>100^{\circ}\text{C}$ ). Significant changes to the MA steels will be required before the air-cooled impact properties will match those of Q&T grades.

#### 1.4 Current State of Understanding Strength-Toughness Relationships

##### 1.4.1 Strength

From a physical standpoint, strength is related to the difficulty of dislocation generation and motion. The harder it is to form and move dislocations, the stronger the material is. Experimentally, strength is evaluated by tensile testing and hardness measurements. A tensile test provides precise information about yielding, strain hardening, and fracture of a material, but is a destructive test. Hardness is a more general parameter that approximates the yield and ultimate strength of a material, and can be applied as a non-destructive test for inspection.

In the literature, equations to predict the mechanical properties of  $\alpha$ -P steel are numerous, but most are strictly empirical in nature and are applicable to a relatively narrow range of compositions and processes. Modeling of strength by a single mechanism is relatively advanced to the point where yield strength (YS) can be described by the relevant physical process. Where multiple strengthening mechanisms are operative, there is no generally accepted model. Recent developments (16,17) have pushed modeling towards a description of the stress-strain diagram.

Gladman and Pickering (18) and Pickering (2) have summarized the literature regarding our understanding and prediction of strength in  $\alpha$ -P steels. A graphical representation of the effect of the

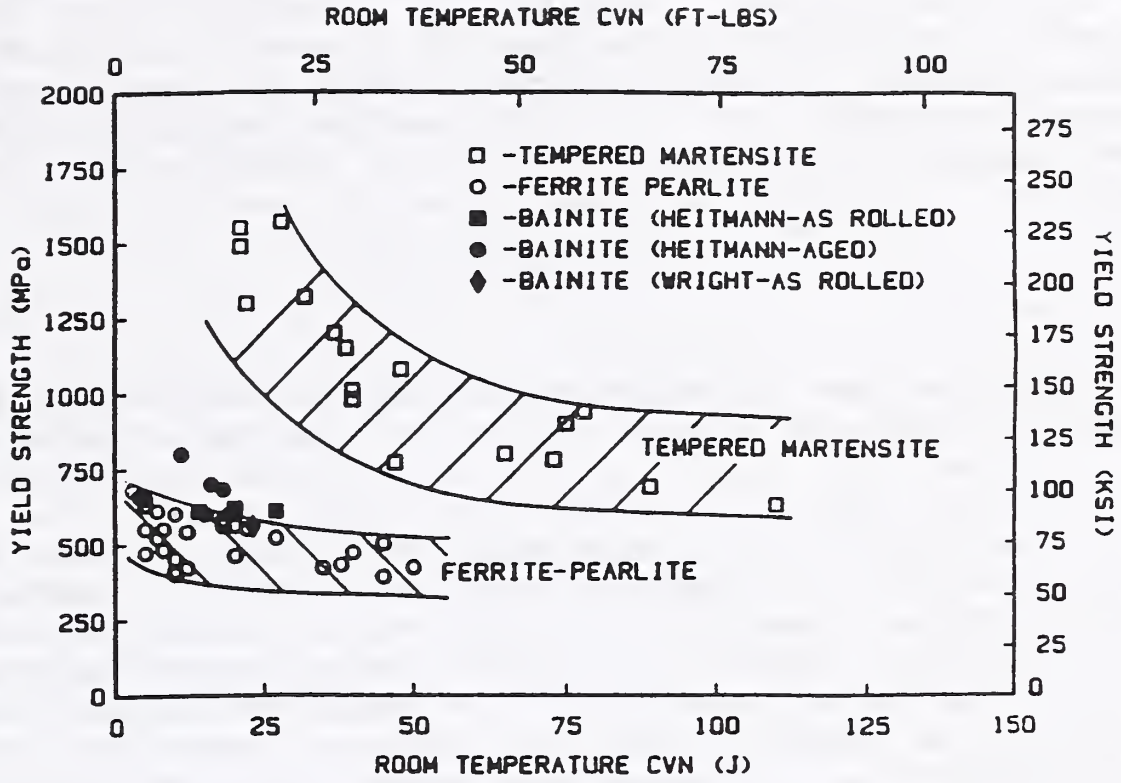


Fig. 2. Plot of YS vs. CVN absorbed energy at room temperature for the two types of steels (14).

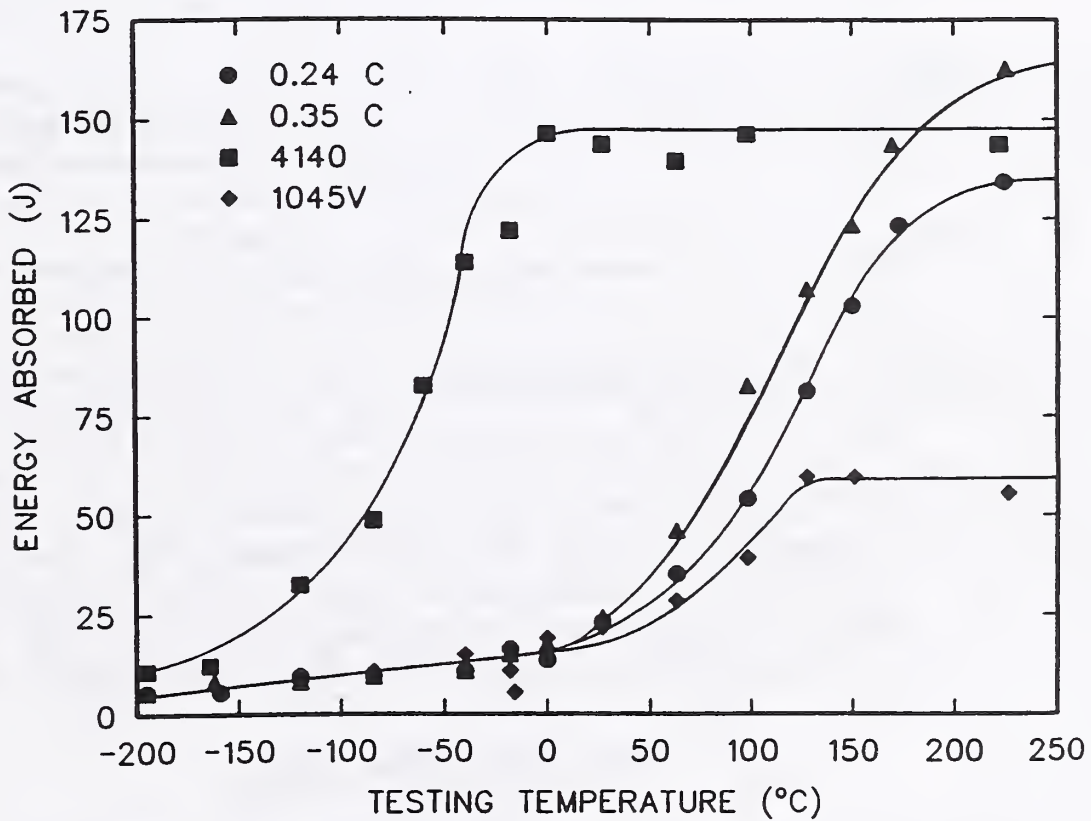


Fig. 3. Plot of CVN absorbed energy vs. temperature for four different types of steels (15).

volume fraction of P on YS is shown in Fig. 4. Ferrite ( $\alpha$ ) grain size and the volume fraction of pearlite  $f(P)$  are the most significant factors influencing YS in  $\alpha$ -P with no MA. YS varies nonlinearly with P content (note that P has practically no effect at fractions less than 0.2). To predict yield strength (YS), the general form of the equation would be as follows

$$YS = \sigma_i + k_y d^{-1/2} , \quad (1)$$

where  $k_y$  and  $\sigma_i$  are the constants from the Hall-Petch equation that describe the effect of grain size,  $d$ , on the strength. The value of  $d$  is generally taken as the macrograin size, but could be a subgrain size under the right processing conditions. The  $\sigma_i$  term is a catch-all for any strengthening mechanism that is operative; the most frequent assumption used is that the effects of different strengthening mechanisms are additive so that  $\sigma_i$  includes  $\sigma_{ss}$ ,  $\sigma_{ppt}$ ,  $\sigma_d$ ,  $\sigma_{tx}$ , and  $\sigma_{tr}$ , where  $\sigma_{ss}$  = solid solution strengthening,  $\sigma_{ppt}$  = precipitation strengthening,  $\sigma_d$  = 'forest' dislocation strengthening,  $\sigma_{tx}$  = a crystallographic texture parameter, and  $\sigma_{tr}$  is the strengthening due to phase transformation. The second part of Eq. (1),  $k_y \cdot d^{-1/2}$  represents the grain size contribution to YS ( $\sigma_{gs}$ ).

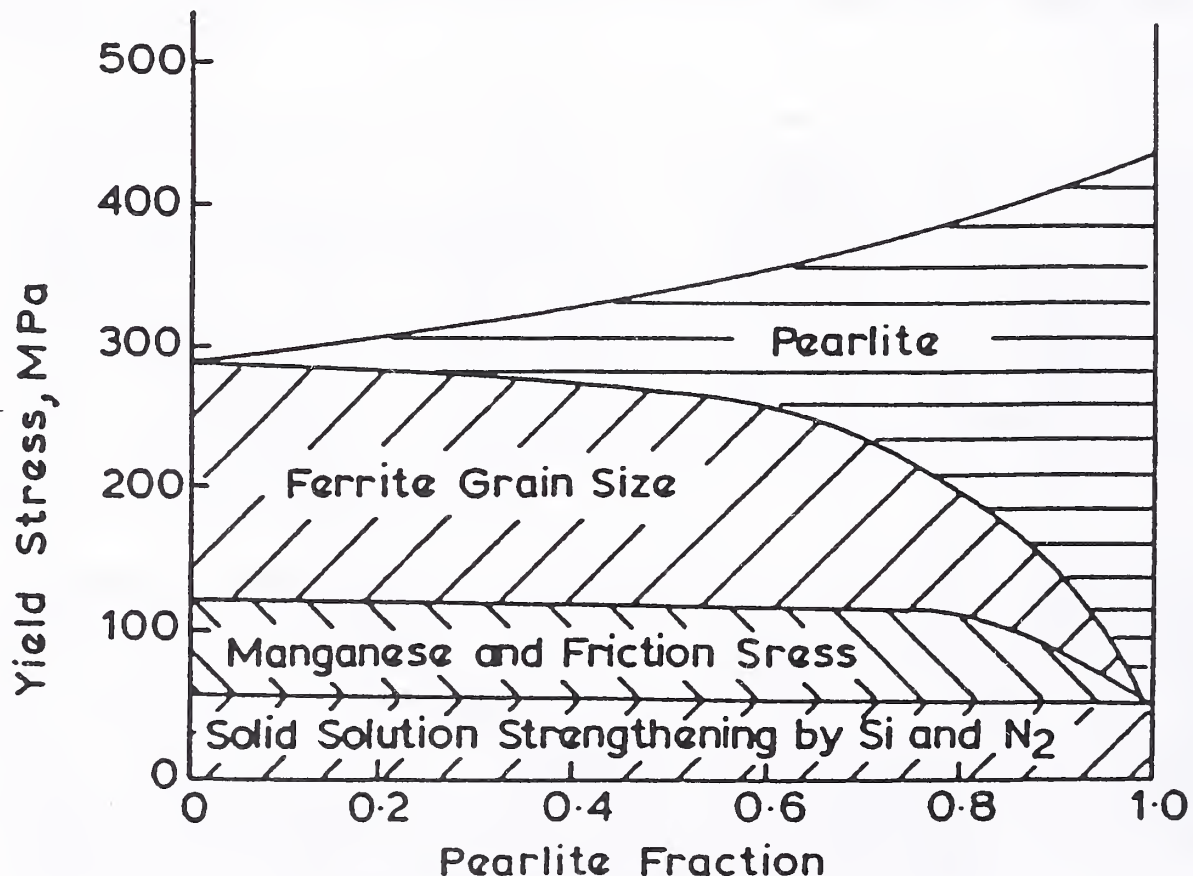


Fig. 4. Schematic diagram showing the contribution of different strengthening mechanisms to the YS of steel as a function of pearlite fraction (18).

#### 1.4.1.1 Effect of Grain Size

Hall-Petch relationships are important in understanding the change in properties, but it can be difficult to employ Eq. (1) quantitatively to a particular system. The measurement of grain size can lead to problems. Even in an equiaxed and uniform grain structure, there is some confusion regarding what is the effective grain size. In most cases, the mean linear intercept,  $d'$ , of grain size measured from the polished cross section of the material is used. However, values of 1.75 to 2 times  $d'$  are sometimes used to account for sectioning effects. Frequently the definition of 'grain size' and sometimes its units are not even reported. These factors contribute to the variation in the reported values of  $k_y$  found in the literature.

The problem of defining the effective grain size to use in a predictive equation, like Eq. (1), is acute when the structure is not uniform or equiaxed. Low C steels were used in the derivation of the Hall-Petch equation and  $d$  referred to the ferrite grain size in the absence of a second phase. For higher C steels where there is a large fraction of pearlite and the ferrite is present as a network around the pearlite, the role of  $d$  in determining the strength is more complicated. The thickness of the ferrite network is the feature that is normally measured to include in Eq. (1). Bainitic and martensitic structures in steels are inherently acicular. Some processing conditions produce a duplex, but equiaxed grain structure while others distort the grain structure in the rolling direction (18).

It should also be noted that the function  $d^{-1/2}$  seems to fit most theories and a large body of data; however, equally significant relationships can sometimes be obtained by using a factor of  $d$  to the  $-1/4$ ,  $-1/3$ , or  $-1$  power (18).

#### 1.4.1.2 Effect of Precipitation

The effect of precipitation can be relatively large in  $\alpha$ -P forging steels; approximately 150 MPa increase in YS is not uncommon. The precipitation occurs by MA elements combining with C and N, and the maximum  $\sigma_{ppt}$  contribution could be estimated from the chemical composition. In theory,  $\sigma_{ppt}$  can be modeled by considering the influence of the particles on the movement of dislocations, commonly referred to as dispersion hardening (19-20). The following equation can be used to describe the increase in YS related to precipitation of V(C,N) particles:

$$\Delta YS = \frac{K[f(ppt)]^{1/2}}{X_{ppt}} \frac{\ln(X_{ppt})}{b}, \quad (2)$$

where  $f(\text{ppt})$  = volume fraction of precipitates and  $x_{\text{ppt}}$  is the mean planar intercept of the spacing between particles in nm.  $K$  is a constant which is nearly  $6 \text{ N/m}$  and  $b$  is the Burger's vector for dislocations (approximately  $0.25 \text{ nm}$ ).

Actual strengthening due to precipitation depends critically upon processing. For example, precipitates containing Nb can form in austenite during hot deformation, which retards recrystallization, or the precipitates can form in ferrite during and/or after transformation, which provides strength at room temperature. If the precipitates form in austenite, they influence the final grain size  $d$ , and therefore YS and CVN results, but not  $\sigma_{\text{ppt}}$ . Data on the variation of precipitation due to processing variables are found in recent work by Leap et al. (21).

Precipitation is generally assumed to have nearly equal effect on strength of  $\alpha$  and P. Sage (5) found that this assumption was not always true. In a steel with  $0.35\% \text{ C}$ ,  $1.1\% \text{ Mn}$ , and a normal N content of  $100 \text{ ppm}$ , precipitation was only found in proeutectoid  $\alpha$  and not in the pearlite phase. For other alloys, precipitates were present in both phases.

The strengthening due to precipitation is usually inferred from direct comparison with the predicted strength for a steel without MA additions (5,22). Figure 5 shows the effect of V additions on the ultimate tensile strength (UTS) of  $0.45\% \text{ C}$  and  $0.8\% \text{ Mn}$  steel (5). The variation in MA had no effect on the volume fraction of ferrite  $f(\alpha)$  and interlamellar spacing  $S_p$ , so it was easy to separate out the effects of MA and phase transformation. The  $\sigma_{\text{ppt}}$  increment increases with the V content at a rate of  $100 \text{ MPa}/0.1\% \text{ V}$ . The scale of the precipitation strengthening (average particle spacing  $L$ ),  $0.03$  to  $0.1 \mu\text{m}$ , is much finer than that which determines the YS of  $\alpha$  and P.

The assumption that  $\sigma_{\text{ppt}}$  adds to other mechanisms has not been proven by fundamental studies in all cases. Theoretical models for  $\sigma_{\text{ppt}}$  are based on the interaction between moving dislocations and the precipitates. If the precipitates are coherent or semi-coherent, the dislocations cut through the precipitates and affect YS much more than the strain hardening and UTS. If the particles are incoherent with the matrix, dislocations will normally bow out around the obstacles and increase strain hardening and UTS as well as the YS. For steels with  $<0.2\% \text{ C}$ , Gladman et al. (23) compared the fundamental mechanisms and found the contributions of  $\sigma_{\text{ppt}}$  from MA precipitates and of grain refinement,  $\sigma_{\text{gs}}$ , were additive.

Hornbogen and Staniek (24) studied  $\sigma_{\text{ppt}}$  due to Cu precipitation in iron and how precipitation affected the sum of  $\sigma_{\text{ppt}}$  to  $\sigma_{\text{gs}}$ . In this case,  $\sigma_{\text{ppt}}$  did add to  $\sigma_{\text{gs}}$  as long as the precipitates were coherent ( $<10 \text{ nm}$  in diameter) with the matrix. When the precipitates grew larger and lost coherency, bowing of dislocations around the

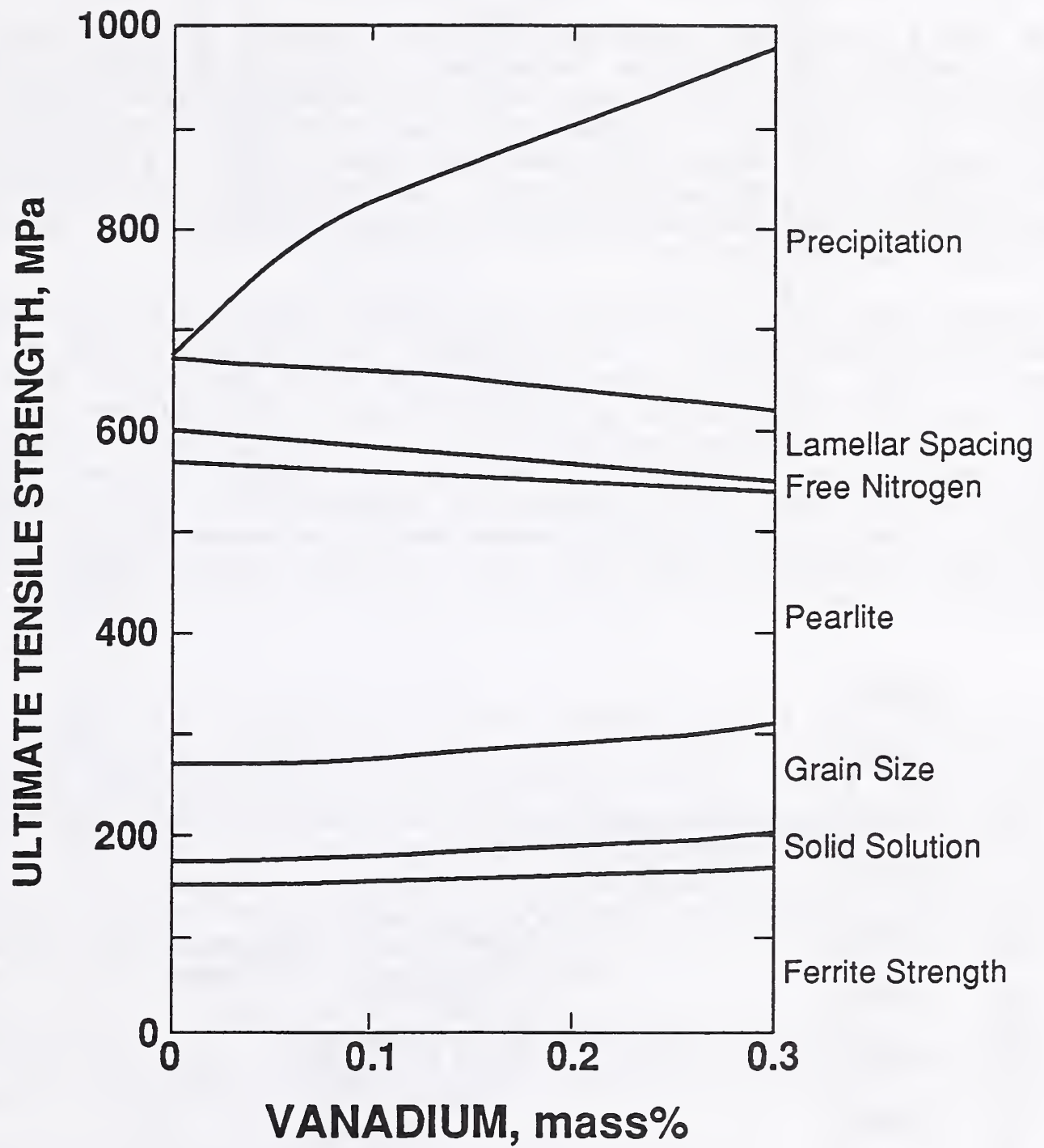


Fig. 5. Schematic diagram showing the contribution of different strengthening mechanisms to the UTS of steel as a function of V content (5).

precipitates was the dominant physical process affecting YS, and the contribution of  $\sigma_{gs}$  was lost.

#### 1.4.1.3 Effect of Phase Transformation

For the air-cooled, medium carbon  $\alpha$ -P steels, the  $\sigma_{tr}$  contribution is a result of pearlite formation. Transformation is typically represented by a continuous cooling-transformation (CCT) diagram, which is directly related to the chemical composition, prior austenite grain size, and cooling rate. Figure 6 shows a typical CCT diagram for SAE 1141-Nb (25). Information from CCT diagrams is essential to understanding transformation phenomenon, which in turn affects the properties.

Probably the most effective way to increase  $\sigma_{tr}$  is to raise the C content of the steel. An increase in C content from 0.1 to 0.6 mass % will increase the f(P) from <15% to about 90% for air cooling of a large (200 mm diameter) bar. The effect of C content on mechanical properties  $\alpha$ -P steels is summarized in Fig. 7 (26). The composition change will result in a nearly linear increase in tensile YS, UTS, and transition temperature in notched impact tests. The increase in C content will decrease both the reduction of area in tensile testing and the upper shelf energy in impact tests.

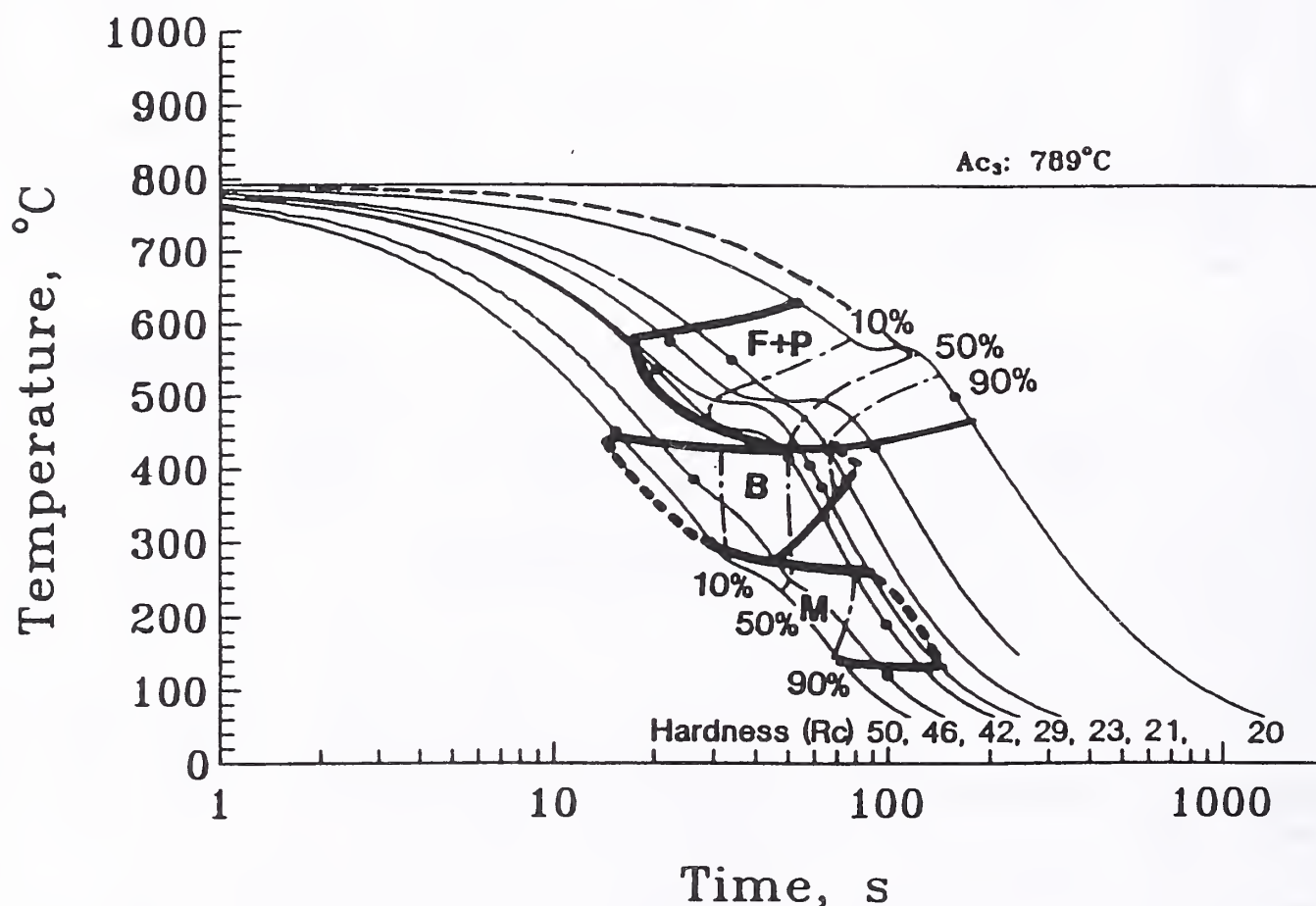


Fig. 6. CCT diagram for SAE 1141-Nb steel (24).

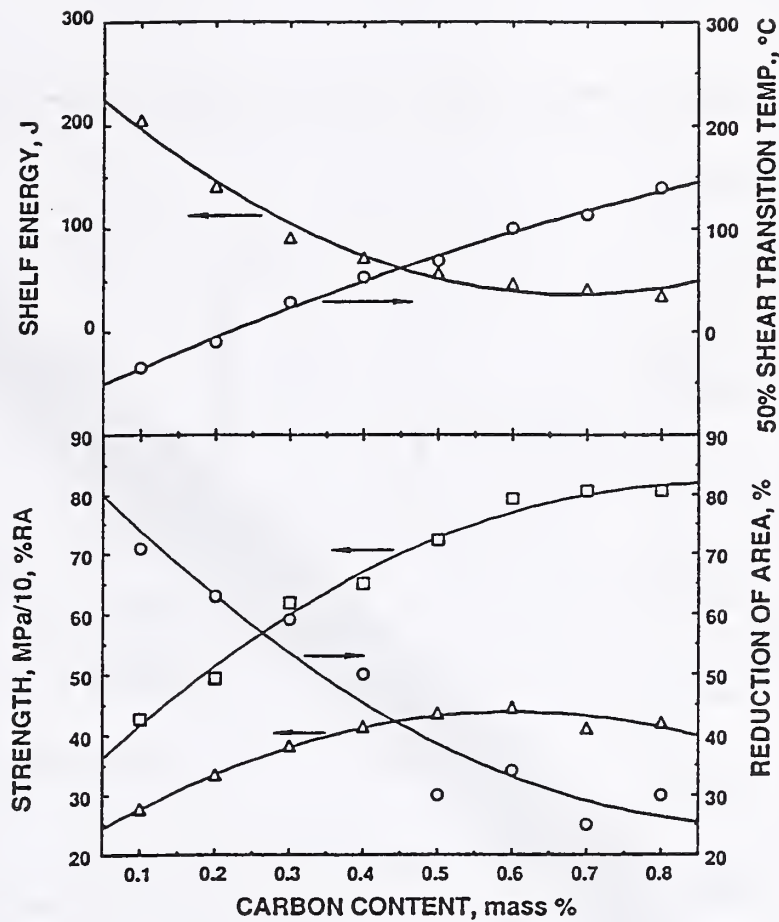


Fig. 7. Effect of C content on mechanical properties of  $\alpha$ -P steels (25).

The most important structural feature that affects the strength of P, for a given C content, is the spacing of the lamellar carbides  $S_p$ . Usually the effect is described by a Hall-Petch type factor where  $S_p^{-1/2}$  is the functional relationship. For eutectoid steel (C content<sup>p</sup> = 0.8 mass %), evidence indicates that a  $S_p^{-1}$  makes more physical sense. Figure 8 shows data from Marder and Bramfitt (27) plotted as a function of  $S_p^{-1}$ , which gives a positive value for  $\sigma_i$ . If the data were plotted as a function of  $S_p^{-1/2}$ ,  $\sigma_i$  for YS would be negative, which makes no physical sense.

Lagneborg et al. (28) reported equations that relate the C and Mn content to  $f(P)$  for steel bars with different diameters  $\Phi$ , which resulted in different cooling rates.

For 200 mm  $\Phi$  ( $dT/dt = 0.2^\circ\text{C/s}$  in still air),

$$f(P) = 1.03 \cdot \%C (1 + 0.74 \cdot [\%Mn]). \quad (3)$$

For 70 mm  $\Phi$  ( $dT/dt = 0.5^\circ\text{C/s}$  in still air),

$$f(P) = 1.18 \cdot \%C (1 + 0.64 \cdot [\%Mn]). \quad (4)$$

For 30 mm  $\Phi$  ( $dT/dt = 1.3^\circ\text{C/s}$  in still air),

$$f(P) = 1.34 \cdot \%C (1 + 0.60 \cdot [\%Mn]). \quad (5)$$

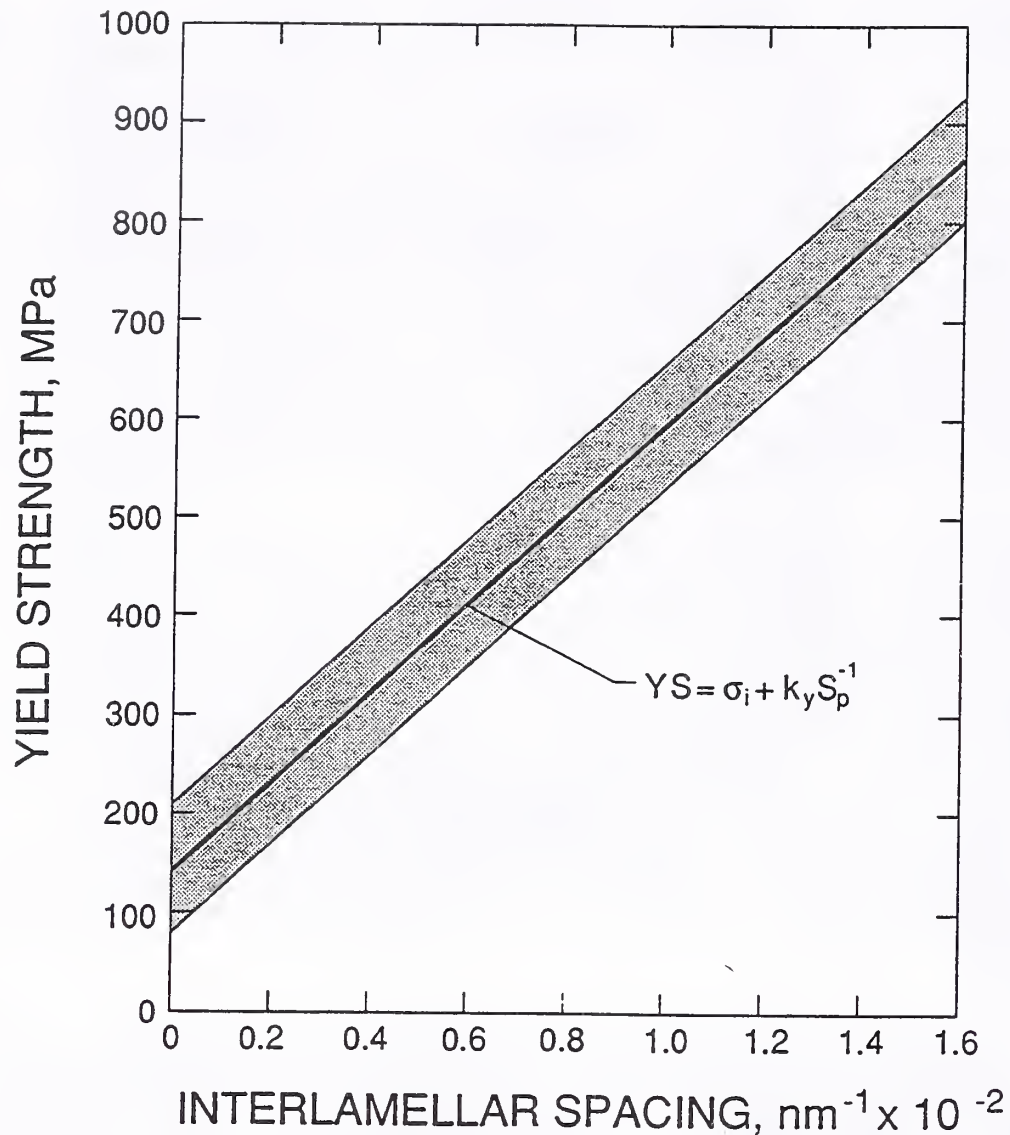


Fig. 8. Effect of interlamellar spacing on YS of eutectoid steel (26).

Depending upon the exact application, it may be necessary to also consider other transformation products like bainite or martensite. Bainite has a higher hardness and strength than a comparable  $\alpha$ -P mixture, but the toughness of bainite can vary quite a bit depending upon the C content and type of bainite. Ollilainen et al., (29) have shown that the lower temperature transformation products in a  $\alpha$ -P steel with V, Cr, and Mn additions and a C content of 0.45 mass % increase strength, but lower the toughness and machinability. For a steel with a lower C content (0.25 to 0.35%), bainite has been shown to improve both strength and toughness (13,30). Given the variation in section size of many forgings, like that shown in Fig. 9, the cooling rate in still air after forging could result in bainite and/or martensite formation in the thinner sections. The CCT diagram is useful in this regard because it will define the cooling rates for which bainite-martensite formation can occur.

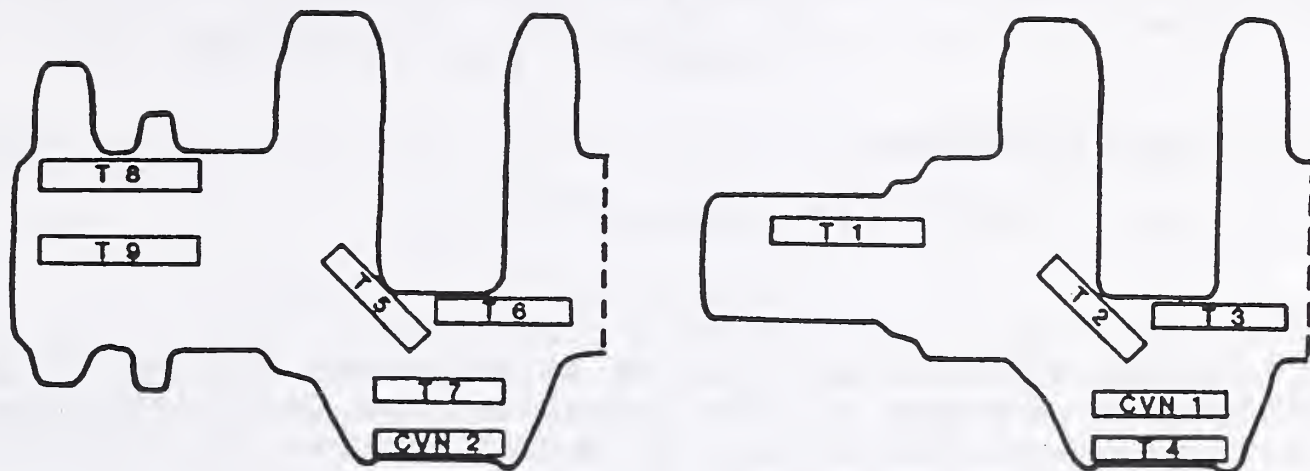


Fig. 9. Schematic diagram of cross sections through two typical forgings. The effective cooling rates for specimens T8 and T9 will be lower than that for specimen T1 due to the different section sizes for the two forgings.

#### 1.4.1.4 Effect of Solid Solution Strengthening

Solid solution strengthening is not as important to YS as grain size, transformation (pearlite content) and precipitation, and is probably more important in terms of hardenability effects on the CCT diagram. Normally  $\sigma_{ss}$  is added to the other terms as a constant times the content of a given element (mass %). The value of the constant is determined empirically, but is related in theory to the lattice distortion that the element produces in the ferrite matrix. Mn and Si are the two most important substitutional alloying elements. The only interstitial element that normally needs to be considered is N. In theory, the Mn and Si can be assumed to be "free" and in solution (in most cases, part of the Mn and Si is actually tied-up as inclusions), but the "free" N content is generally assumed to be zero when MA elements are present.

#### 1.4.1.5 Effect of Texture and Dislocations

These two factors are relatively unimportant for the type of forging steels discussed here.

#### 1.4.1.6 Summary of Strength Effects

Gladman and Pickering (18) have summarized the results of numerous tests on  $\alpha$ -P steels without MA and interpreted the data in terms of the effects of different strengthening mechanisms. Statistical,

multiple-regression analysis of the data produced the equations shown below that predict YS reasonably well ( $\pm 48$  MPa):

$$\begin{aligned} \text{YS} = f(\alpha)^{1/3} \cdot \{35 + 58(\text{mass \% Mn}) + 17.4 \cdot d^{-1/2}\} \\ + [1-f(\alpha)^{1/3}] \cdot \{178 + 3.8 \cdot S_p^{-1/2}\}. \end{aligned} \quad (6)$$

and a slightly simpler

$$\begin{aligned} \text{YS} = f(\alpha)^{1/3} \cdot \{35 + 17.4 \cdot d^{-1/2}\} \\ + [1-f(\alpha)^{1/3}] \cdot 178 + 3.8 \cdot S_p^{-1/2}, \end{aligned} \quad (7)$$

where  $f(\alpha)$  is the volume fraction of polygonal ferrite,  $S_p$  is the interlamellar spacing of the pearlite and the microstructural features are measured in mm. YS varies nonlinearly with  $f(\alpha)$  and has been described by a modified rule of mixtures involving an exponent of 1/3 on the volume fraction of proeutectoid  $\alpha$  phase. The factors controlling YS of the individual components are on different scales. For  $\alpha$ , YS is largely a function of the grain size, which is typically in the 5 to 50  $\mu\text{m}$  range. For P, YS is a function of the inverse square root of  $S_p$ , which can vary from about 0.1 to 0.4  $\mu\text{m}$ .

Burnett (31) used a regression analysis to describe YS of MA  $\alpha$ -P steels by forging parameters and chemical composition over a limited range of variables. The equation is shown below:

$$\text{YS} = 87.7 + 170(\% \text{Mn}) + 58.3(\text{Ln } (dT/dt)), \quad (8)$$

where  $dT/dt$  is in  $^{\circ}\text{C}/\text{min}$  and  $\% \text{ Mn}$  is in mass  $\%$ . There was excellent agreement between measured and calculated values (0.99 R-square and 95% confidence band is  $\pm 20$  MPa), but it does not address the fundamental factors ( $\sigma_{gs}$ ,  $\sigma_{ppt}$ , and  $\sigma_{tr}$ ) that contribute to YS.

There have been many attempts to relate a Hall-Petch type relationship between grain size and either hardness or flow stresses at higher strains (32). Such relationships have to be viewed with skepticism from a theoretical standpoint because the strain-hardening effects are complex and difficult to model except for specific examples.

For the UTS of  $\alpha$ -P steels without MA, Gladman and Pickering (18) report an equation, similar to Eq. (7) for YS, that is shown below:

$$\begin{aligned} \text{UTS } (\pm 50 \text{ MPa}) = f(\alpha)^{1/3} \{246 + 18.2 \cdot d^{-1/2}\} \\ + [1-f(\alpha)^{1/3}] \{720 + 3.5 \cdot S_p^{-1/2}\}. \end{aligned} \quad (9)$$

Equation (9) describes 96% of the data.

Lagneborg et al. (28) have pointed out that the UTS is more important than YS for evaluation of MA  $\alpha$ -P steels in automotive applications because it relates better to component performance, like fatigue resistance. Therefore, they propose an equation,

$$\text{UTS} = 177 + 533 \cdot \{f(P) + (2.2 + 0.71 \cdot \log_{10}[dT/dt]) \cdot (5 \cdot N + V) + 0.12 \cdot \text{Si}\} , \quad (10)$$

where  $f(P)$  is the volume fraction of P, N, Si, and V are in mass % and  $dT/dt$  is the cooling rate at 750°C in °C/sec. The terms for cooling rate, N, and V are related by the kinetics of transformation directly to the size and volume fraction of precipitation.

Even though Eq. (10) for UTS has no fundamental relationship to theory, it certainly is easy to use because it incorporates precipitation effects through the cooling rate and composition terms, rather than in terms of structural features. The comment about the significance of YS to the application is well taken. Equation (10) does not incorporate any terms related to  $S_p$ , probably because the variation in  $S_p$  normally found in air-cooled steels has relatively little effect on UTS. The equation also allows for tradeoffs between strengthening mechanisms, e.g., reduced P content can be made up by increased cooling rates and/or higher V and N contents, which produce more precipitation strengthening.

Several potential problems are inherent with the statistical, multiple-regression analysis of test data, which considers the strengthening mechanisms as additive, like those published by Gladman and Pickering (18) and Lagneborg et al. (28). Often there is doubt as to whether truly independent variables have been considered in the analysis. The size scales over which the strengthening mechanisms operate may dictate that one mechanism will dominate over the others.

#### 1.4.2 Hardness

Hardness is dependent upon P content and precipitation because it is really associated with plastic flow just like the ultimate strength. Standard Rockwell tests with C or B scales and Brinell tests are macroscale hardness measurements because the size of the indentation and the locally deformed area are generally greater than the size of the microstructural features. The hardness is an average over all of the features. Vickers and Knoop hardness tests are microhardness scales because the size of the indentation is similar to the size of the microstructural features.

Correlation between hardness and tensile properties can be made for specific grades, like SAE 1141. These types of correlations are

extremely valuable when comparing steels with similar composition, but trouble is expected when the correlations are extended to different alloys or the same alloy but with different microstructures.

#### 1.4.3 Toughness

After strength, the major issue related to forging steels is toughness. The physical phenomena related to toughness are more complex than that considered for strength. At lower temperatures and higher strain rates, resistance to cleavage is important. Near ambient temperatures and at slow strain rates, microvoid coalescence is important. For cyclic loading, the formation of fatigue striations leads to failure.

##### 1.4.3.1 Impact Testing

The most frequently used toughness evaluation in industry is the CVN impact test. Figure 3 showed the results of CVN testing from different types of steel over the range of temperatures where the fracture mode changes from ductile to brittle. For forging steels, the common measure of toughness is the ductile-brittle (cleavage) transition temperature (DBTT). There are several ways to define DBTT, but the most common way and the way used here is the temperature at which the energy absorbed during the test is 27 J (20 ft lb). In general, the DBTT as well as the upper and lower shelf energies may be important.

Of the three parameters that can be used to characterize CVN testing (DBTT, upper shelf energy, and lower shelf energy), microstructure has the biggest effect on DBTT, and as a result, DBTT has been studied extensively (33-35). Again, similar to the empirical modeling that has been done for strength, grain size is an extremely important factor affecting DBTT. The effect of  $\alpha$  grain size, or the P colony size  $p$ , on DBTT is due to an increasing difficulty in propagating a cleavage crack as the grain size decreases. Each time a crack encounters a high-angle grain boundary, the crack has to re-orient itself. Experimental evidence has shown that grain boundaries can stop a crack so that it must re-nucleate at a second location. The value of  $p$  is determined by the prior austenite grain size  $D$  and to a lesser extent by the cooling rate.

The energy absorbed in a CVN test at room temperature for a MA  $\alpha$ -P steel is generally in the transition region (see Fig. 3) (15). A higher resistance to ductile fracture, or a lower resistance to cleavage fracture will change the transition region and could influence the results. At a given value of austenite grain size, toughness is increased by a lower C content (more  $\alpha$ , less P), and more P dilution (increasing the cooling rate and Mn content), but these effects are secondary in comparison to that of  $D$  and  $p$ . Given the complex interactions between microstructural constituents, CVN testing at room temperature may not be a

clear-cut way to characterize impact toughness. The whole transition curve is valuable for a better evaluation.

The energy absorbed during impact testing at temperatures below DBTT, referred to as the lower shelf energy, is related to cleavage fracture on {100} planes in ferrite. Microstructural effects on the lower shelf energy are of little interest in the technical community because the absolute value of the absorbed energy is low (<5 J), so that even large relative effects are insignificant.

The energy absorbed during impact testing at temperatures above DBTT, referred to as the upper shelf energy, is related to ductile fracture by microvoid coalescence at second-phase particles in the structure and can vary significantly with microstructure. The most important factors to consider are the volume fraction of second phase and strength, which are largely determined by the  $f(P)$  and precipitation. Figure 7 (26) showed how increases in C content, which determines the  $f(P)$ , improves the strength, but lowers toughness (reduction in area (RA) goes down, DBTT goes up, and the upper shelf energy is lower).

The effects of structure on DBTT for  $\alpha$ -P steels have been described by a simple rule of mixtures that incorporates each constituent. Gladman and Pickering (18) give the following equations to predict the DBTT:

$$\begin{aligned} \text{DBTT } (\pm 30^\circ\text{C}) = & f(\alpha) \cdot [-46 - 11.5 \cdot d^{-1/2}] + (1 - f(\alpha)) \cdot [-335 \\ & + 5.6 \cdot S_p^{-1/2} - 13.3 \cdot p^{-1/2} + (3.48 \times 10^{-6}) \cdot t], \end{aligned} \quad (11)$$

that explains 82% of the data. There are complex interactions for the microstructural constituents, i.e.,  $p$ ,  $d$ ,  $S_p$ ,  $f(\alpha)$ , and carbide thickness  $t$ , which are not apparent from Eq. (11). Decreasing  $t$  requires  $S_p$  to increase, so that the rate of change in DBTT is not independent of the two factors. For a given C content, the relationship between  $t$  and  $S_p$  can be described by the following equation (36,37):

$$t = S_p / \{ [f(P) / 0.15 (\% \text{ C})] - 1 \} . \quad (12)$$

The influence of  $p$ ,  $f(P)$ , and  $d$  on DBTT are illustrated in Fig. 10. Higher  $f(P)$  increases DBTT by reducing the influence of  $\alpha$  grain size in the first term in Eq. (11). It is important to note that the effect of  $\alpha$  grain size on the CVN test is large even in the absence of P, see Fig. 10 where the DBTT at zero  $f(P)$  for the two initial grain sizes differ by nearly 50°C.

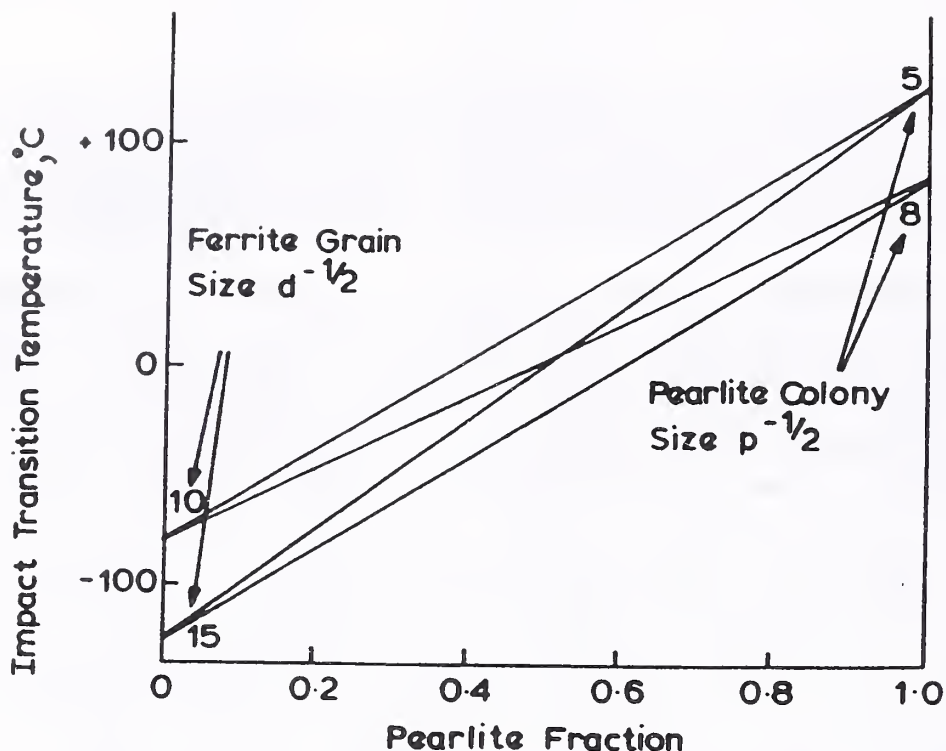


Fig. 10. Interaction between pearlite fraction, pearlite colony size ( $\mu\text{m}$ ), and ferrite grain ( $\mu\text{m}$ ) size on the DBTT in  $\alpha$ -P steels (18).

Strength has a large effect on DBTT, but is not specified in Eq. (11) because strength depends on the same structural factors that influence DBTT. If the equations for YS and DBTT are considered together, then the DBTT will increase by about  $0.3^\circ\text{C}/\text{MPa}$  increase in YS.

Recent developments in Japan have shown that impact toughness can be improved by intragranular  $\alpha$  formation in free machining (high S) steels that also contain V (38). Figure 11 shows the energy absorbed in a Charpy U-notch impact test as a function of temperature for three different steels: air-cooled 0.25C-1.5Mn-0.07S-0.1V steel, air-cooled 0.25C-1.5Mn-0.02S-0.1V steel, and a Q&T 0.45C-0.8Mn-0.02S steel. The air-cooled, high S, V steel is significantly better than the low S version, and slightly better than the Q&T steel at all temperatures. It is important to note that the results from a U-notch test can be different from a standard CVN test due to the lower stress concentration at the notch (compare the differences between the results shown in Figs. 3 and 11).

In the USA, Kirby et al. (37) have shown a lower DBTT (better toughness) in CVN tests for a high S, V, 0.4C steel compared to a similar steel without high S or V, but the trend does not appear as significant as suggested by U-notch results shown in Fig. 11. The mechanism responsible for the increase in toughness is still being studied, but it appears that the high S and V content changes the transformation kinetics for proeutectoid  $\alpha$ . The higher toughness is related to grain refinement and increased  $f(\alpha)$ , and could be described by an equation similar to Eq. (10).

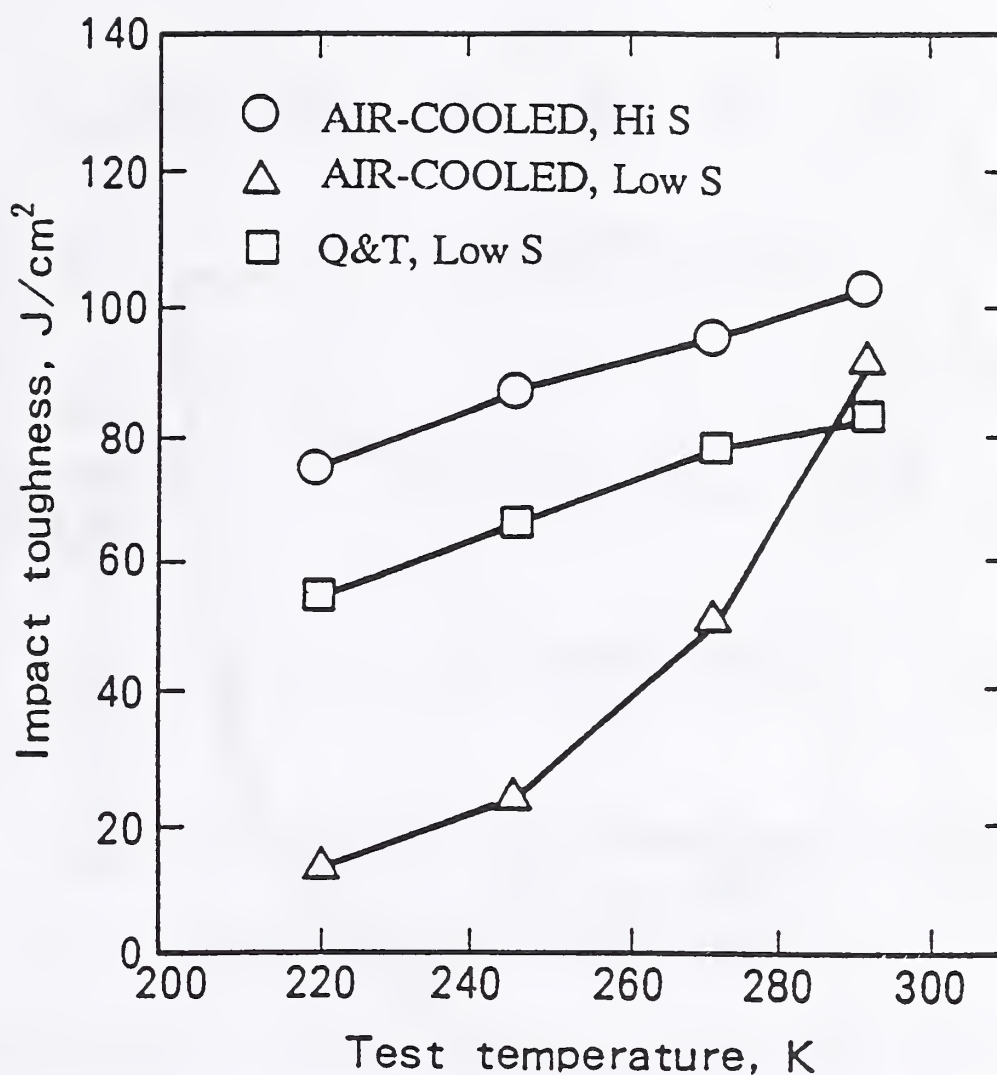


Fig. 11. U-notch impact toughness of steels as a function of test temperature (35).

#### 1.4.3.2 Fracture Toughness Testing

Fracture toughness ( $K_{Ic}$ ) testing is a well-known technique used to evaluate toughness of materials, and was developed as a tool to determine the fitness-for-purpose of a particular material and processing, given the service operating stress and existing flaw size. However,  $K_{Ic}$  testing has not been used routinely for characterization of materials, except for critical safety applications.  $K_{Ic}$  testing is expensive, and it takes a relatively large specimen to get good results.

Limited  $K_{Ic}$  testing has been used to compare MA  $\alpha$ -P to Q&T steels. Ollilaninen et al. (29) found that  $K_{Ic}$  was four times higher for Q&T steels compared to MA  $\alpha$ -P steel at a YS of 650 MPa. The difference in  $K_{Ic}$  between the two steels was not considered significant for many applications because  $K_{Ic}$  did not change the fatigue life, the limiting failure mode, considerably. A schematic diagram illustrating the fatigue behavior for Q&T vs. MA  $\alpha$ -P steels is shown in Fig. 12. Given the fact that most of the fatigue life

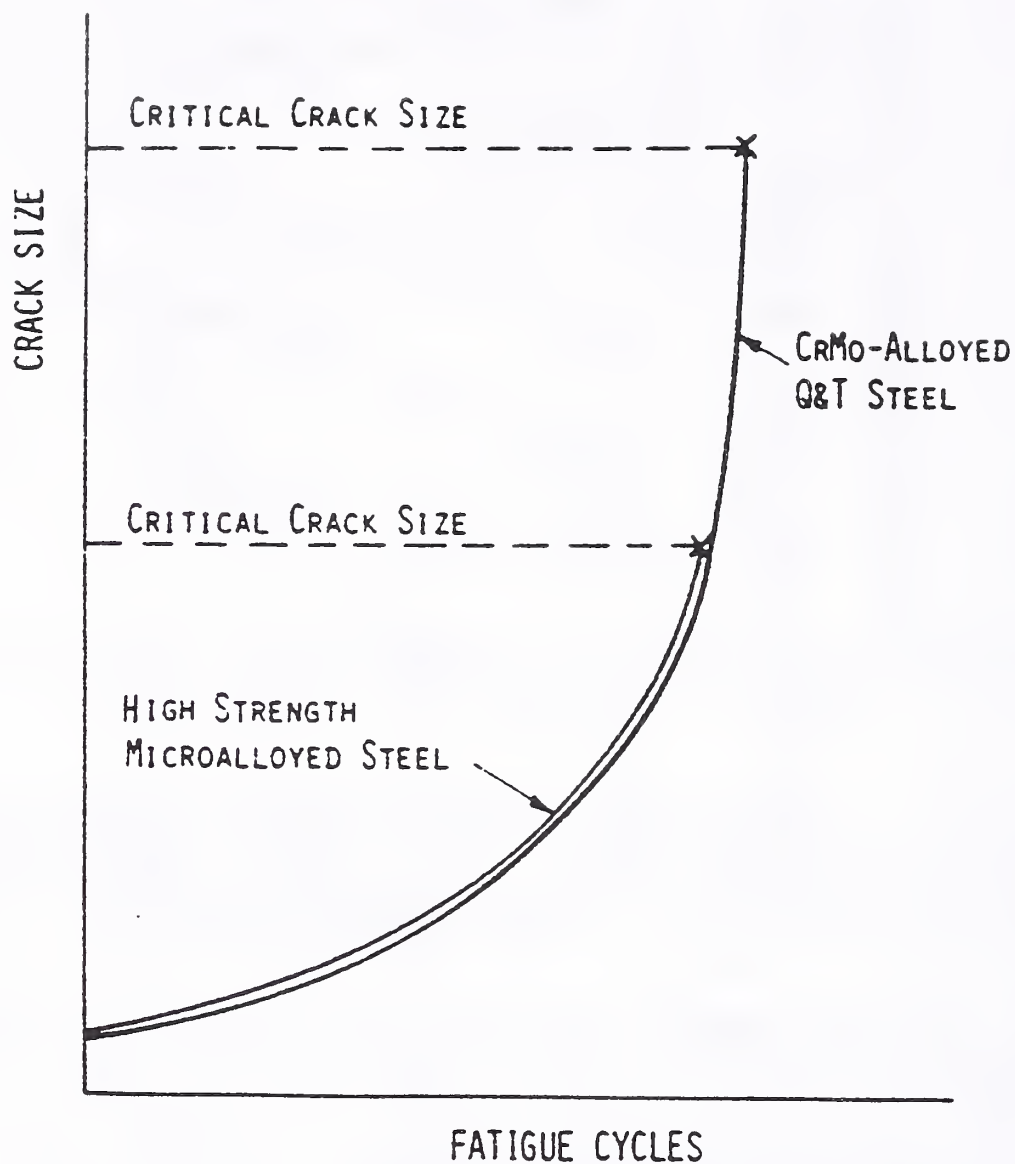


Fig. 12. A schematic curve of the fatigue crack growth and final fracture of high-strength MA  $\alpha$ -P steel and Q&T steel (29).

is consumed with initiation of crack growth, the difference in number of cycles to failure is rather small compared to the difference measured in  $K_{Ic}$ .

Efforts to relate  $K_{Ic}$  from other mechanical properties have been attempted ever since fracture mechanics became accepted in the technical community. Figure 13 shows  $K_{Ic}$  for different MA  $\alpha$ -P steels plotted against the UTS for different steels (9). The correlation between  $K_{Ic}$  is not encouraging. There does appear to be a minimum value of  $K_{Ic}$  of about  $50 \text{ MPa}\cdot\text{m}^{1/2}$  for these types of steels.

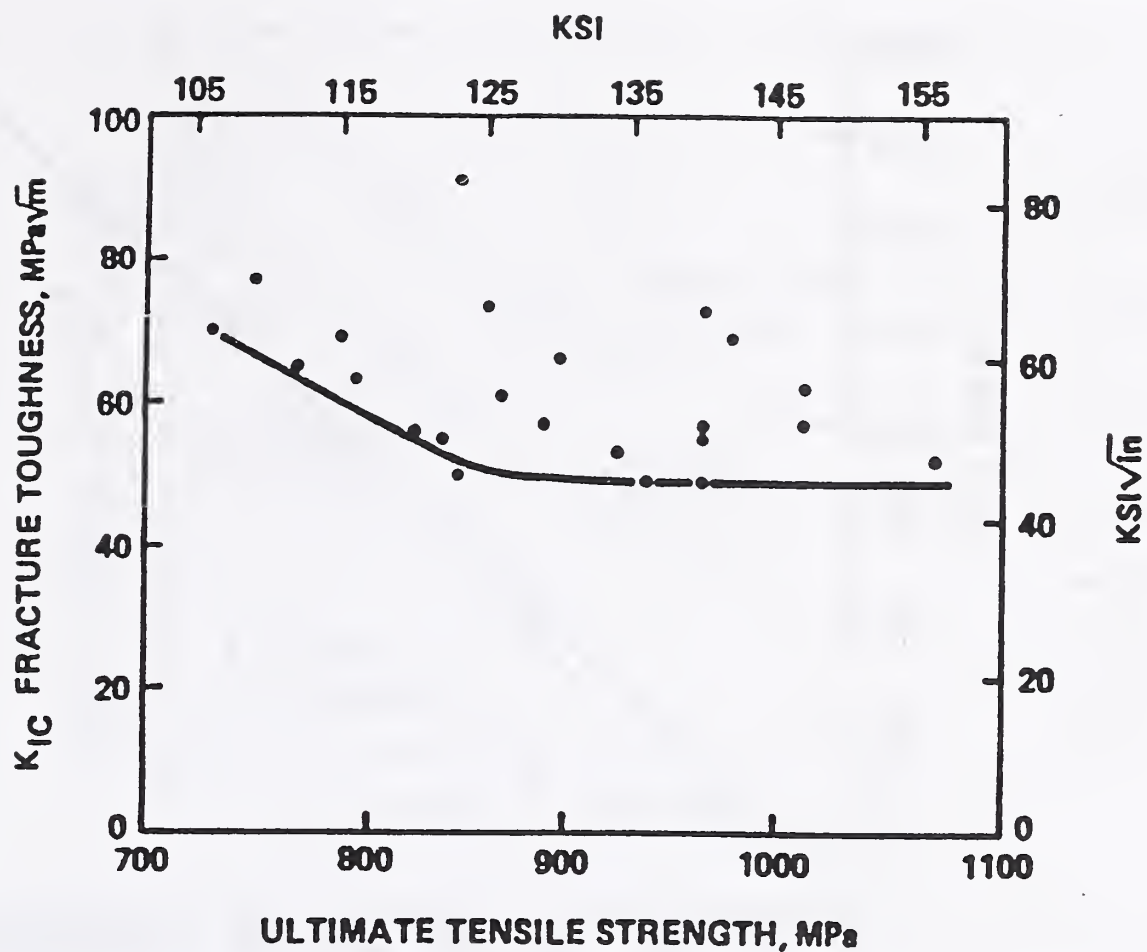


Fig. 13. Correlation between fracture toughness and UTS for  $\alpha$ -P steels (9).

Short-rod, chevron-notch fracture toughness ( $K_{Iv}$ ) testing is a relatively new development in fracture mechanics that has several advantages compared to standard fracture toughness testing. First, the specimen is 2.5x smaller than that required for compact tension testing of ASTM E 399 plane strain fracture toughness. There is no fatigue precracking required for the test as in other fracture toughness test procedures. Past experience (30,39,40) has shown that  $K_{Iv}$  has excellent potential for use as a screening test to evaluate high-strength aluminum alloys and steels. Figure 14 shows a excellent correlation between  $K_{Ic}$  and  $K_{Iv}$  for Q&T steels at room temperature.

#### 1.4.3.3 Tensile Testing

At present, little notice is given to the fracture event of a tensile specimen; typically, the actual fracture load is not even recorded for a test. Of the commonly reported information from a tensile test, only the percent reduction in area (RA) and to a lesser degree, elongation are influenced by fracture. Neither of

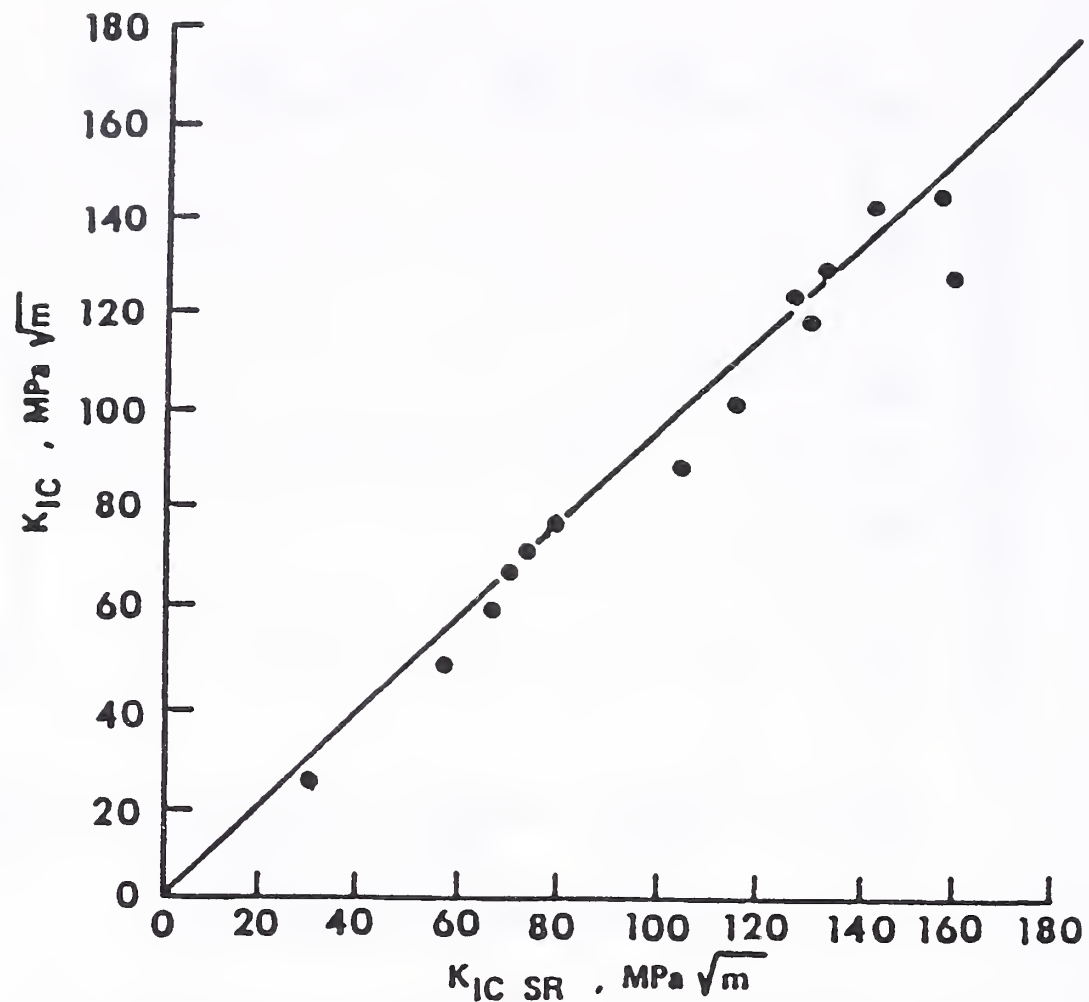


Fig. 14. Correlation between fracture toughness of Q&T steels determined with a compact tension and a short rod specimen (9).

these properties has received much attention in the literature compared to the extensive work done on YS and UTS.

Figure 15 shows the effect of second-phase particles, volume fraction and shape, on fracture strain (23). The true strain to fracture  $\epsilon_f$  and %RA decrease with an increase in volume fraction of second-phase particles. Spherical particles are less detrimental to ductility than elongated or plate-like particles.

Figure 16 shows  $\epsilon_f$  plotted against the upper shelf CVN energy (18). A good correlation is found between tensile and impact test results. Figure 17 shows the true strain plotted vs.  $f(P)$ . Most of the strain is concentrated in the neck as nonuniform strain. There is an exponential decrease in both the uniform strain  $\epsilon_u$  and  $\epsilon_f$  with increasing  $f(P)$ .

Pickering (41) reported the following equation to predict the tensile ductility from the microstructure of  $\alpha$ -P steels:

$$\%RA = 78.5 + 5.39(\%Mn) - 0.53(\% P) - 0.328(d) , \quad (13)$$

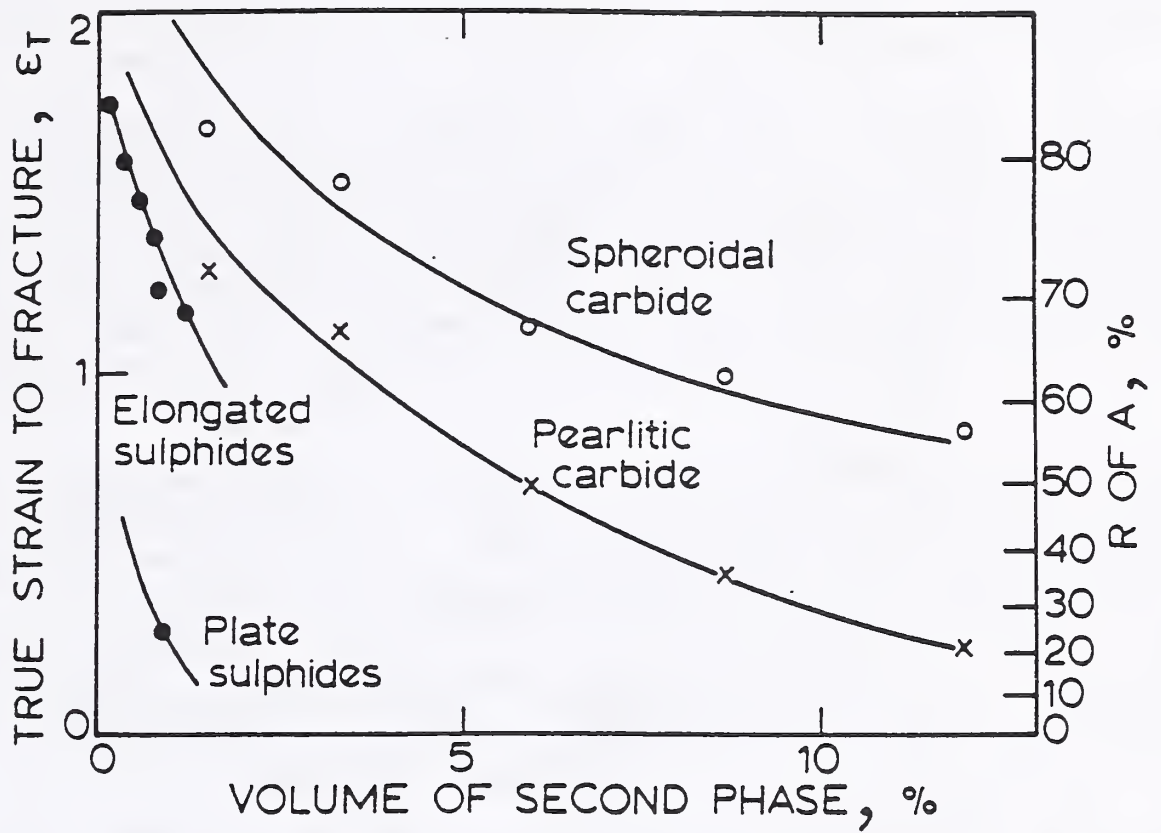


Fig. 15. Effect of second-phase particles and their morphology on total ductility in uniaxial tension (22).

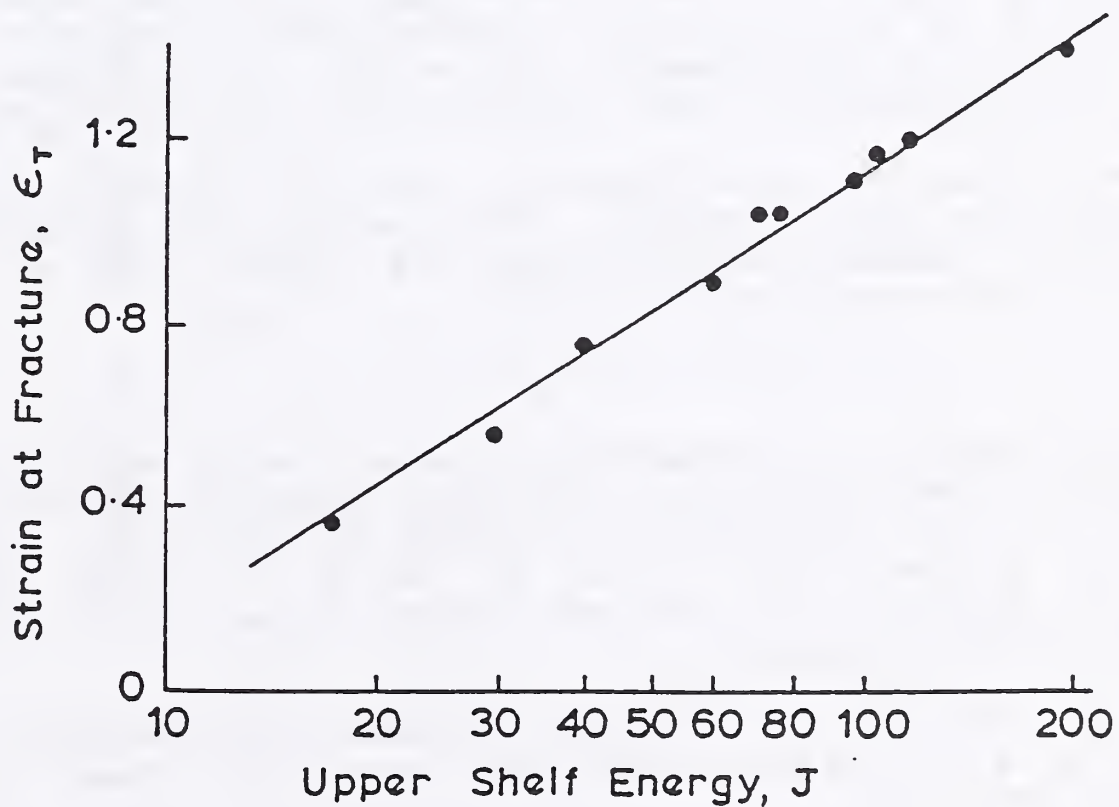


Fig. 16. Plot of true fracture strain in uniaxial tension vs. upper shelf energy absorbed in CVN test (18).

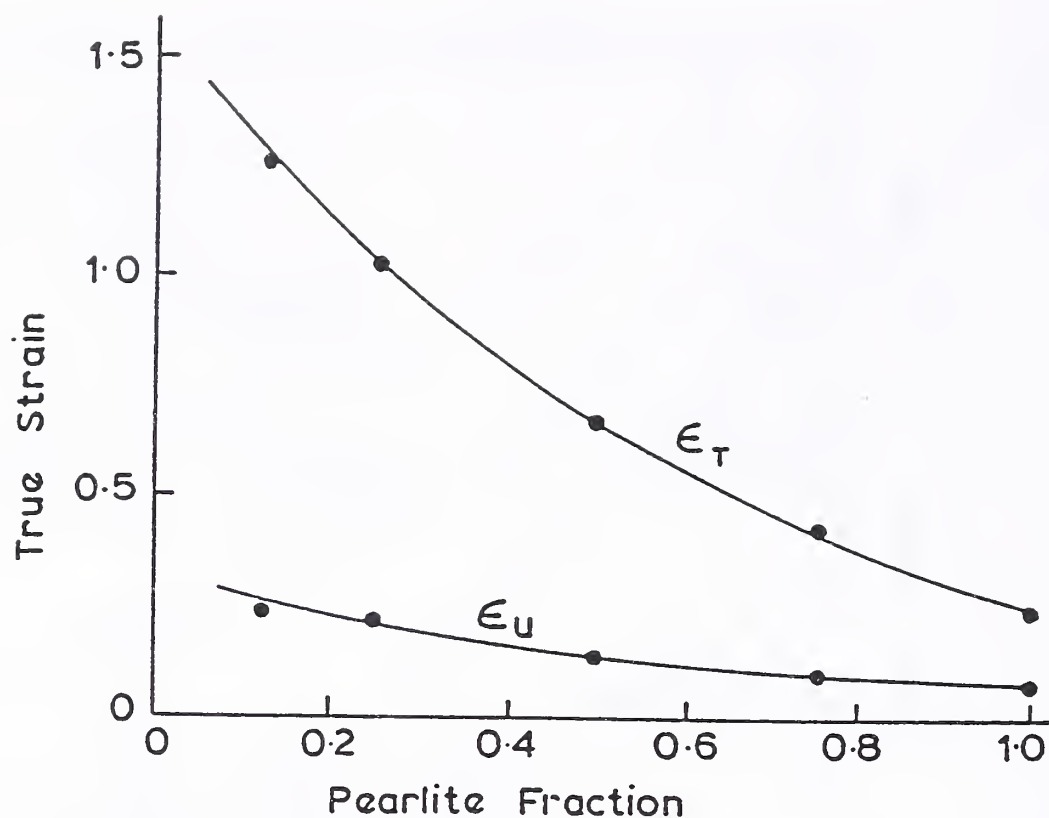


Fig. 17. Effect of pearlite fraction on the uniform,  $\epsilon_U$ , and fracture strain,  $\epsilon_T$ , in uniaxial tension for  $\alpha$ -P steels (18).

where  $d$  is the mean linear intercept grain size in micrometers. From the few reports in the literature, grain size seems to have a large effect on %RA. An order of magnitude decrease in grain size from 100 to 10  $\mu\text{m}$  increases the %RA by 30%. Ollilaninen (29) shows a similar dependence of %RA on grain size for MA  $\alpha$ -P steels.

In terms of the fracture stress  $\sigma_{fr}$ , the only data available in the literature are for eutectoid steels with 100% pearlitic microstructures. Gladman and Pickering (18) report that  $\sigma_{fr}$  is related to  $S_p$  by a Hall-Petch relationship

$$\sigma_{fr} = 790 + 8.5 \cdot S_p^{-1/2} . \quad (14)$$

The relationship is interesting because the constant term in the Hall-Petch relationship,  $\sigma_i$ , increases from 178 MPa for YS, to 550 MPa for  $\epsilon = 0.15$ , and then to 790 MPa for fracture. The coefficient for  $S_p$  goes from 3.8 at YS, 10 at  $\epsilon = 0.15$ , and 8.5 for fracture. The trend is towards higher values of  $\sigma_i$  and  $k_y$  in Eq. (1) for increasing strain.

Marder and Bramfitt (27) found a similar relationship between  $S_p$  and  $\sigma_{fr}$  in a tensile test of 100% pearlitic steel, but with a different exponent:

$$\sigma_{fr} = 436 + 9.81 \cdot S_p^{-1} , \quad (15)$$

where stress is in MPa and spacing is in nm. Again, in this case, a better fit to the data was obtained for  $S_p^{-1}$  compared to  $S_p^{-1/2}$ .

The optimum microstructure needed to maximize  $\sigma_{fr}$  has not been determined. The  $Fe_3C$  constituent in P is the main contributor to the volume fraction of second phase particles in MA forging steels, so we know that we need to minimize the carbide phase in order to obtain the highest possible %RA (Fig. 15). But a high  $f(P)$  is needed to raise the flow stresses (Fig. 4). There should be an optimum P configuration,  $t$  and  $S_p$ , for a given C content that optimizes  $\sigma_{fr}$  and %RA.

A modified Bridgman analysis of the stresses found in a tensile specimen has been proposed as a means of characterizing the toughness of a tensile specimen (42). The sum of the equivalent plastic flow stress  $\sigma_o$  and hydrostatic stress  $\sigma_r$  represents an approximation of the critical stress  $\sigma_c$  required to nucleate the majority of voids that are found on the fracture surface. Figure 18 shows the results of the analysis on a series of tests at different temperatures run on an austenitic stainless steel with two processing histories. The analysis allows the degree of sensitization to be quantified in a simple manner. The critical stress for void nucleation can be used as a failure criterion, one which is linked to the physical process related to fracture, for stress analysis of components in more complex stress states (43).

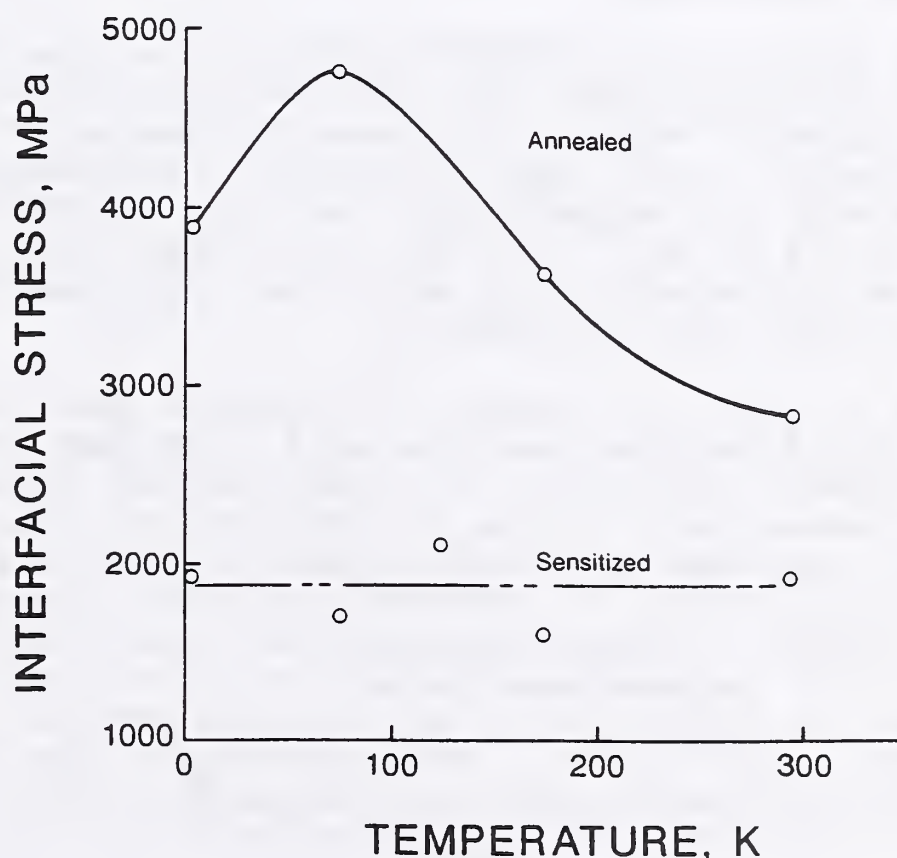


Fig. 18. Plot of interfacial stress at fracture in uniaxial tension vs. test temperature for two austenitic stainless steels, annealed and sensitized (42).

To summarize the effects of microstructure on fracture in uniaxial tension, there is limited evidence that fracture properties are sensitive indicators of microstructural features, just like YS and UTS. In the future, correlations between tensile fracture properties vs. fracture toughness and fatigue resistance are needed. With additional experience, tensile fracture properties could be more valuable.

#### 1.4.3.4 Fatigue Testing

Fatigue is the typical failure mode for many forged, automotive components, but fatigue testing is not the main procedure for characterizing materials and processing. The reason that fatigue testing is not more prevalent to characterize materials and processing effects is because fatigue testing is expensive and time consuming, and the results are sensitive to the applied stress level. The stress concentration due to the design of a component and the tensile properties are both critical factors that determine fatigue life. Designers usually depend upon correlations between tensile properties or hardness and fatigue life to predict a material's fatigue life in the preliminary stages. Then fatigue testing is often performed in the final stages of development on the actual components after the material and processing schedule decisions have been made.

Hardness and UTS are the most important factors related to the endurance limit for fatigue (the stress range required for a life of  $10^6$  load cycles). Figure 19 shows the correlation between the fatigue endurance limit and hardness. Hardness and UTS are influenced mainly by precipitation and  $f(P)$ , which in turn are controlled by chemistry and cooling rate. Typically, the endurance limit for a MA  $\alpha$ -P steel is no more than 10% less than that for a Q&T steel with the same hardness.

The behavior of MA  $\alpha$ -P steels in fatigue has been studied in strain-controlled fatigue tests as well as stress-controlled tests for the endurance limit (9). A comparison of typical cyclic and monotonic stress-strain curves for MA  $\alpha$ -P steel and Q&T steel is shown in Fig. 20. The Q&T steel exhibits cyclic softening while the stress-strain curve for the MA  $\alpha$ -P steel changes little with cyclic deformation. In applications where there is cyclic loading, cyclic stability compensates for a lower monotonic stress-strain curve. Figure 21 shows typical strain-life fatigue curves for a MA  $\alpha$ -P steel and a Q&T steel. The curves for the two steels are similar, although the MA steel was slightly harder.

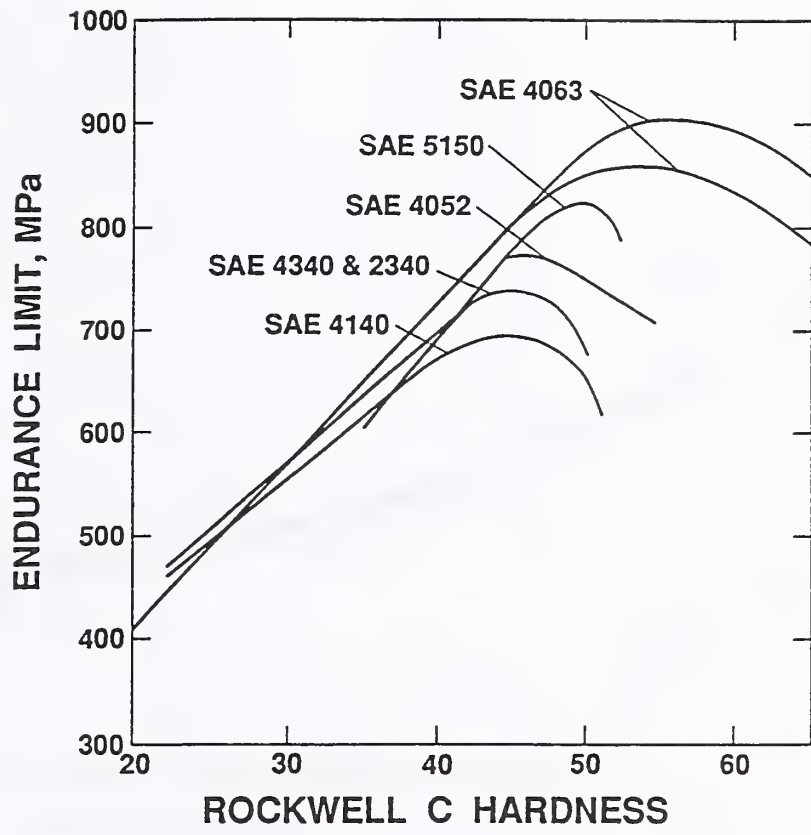


Fig. 19. Correlation between fatigue endurance limit and hardness (19).

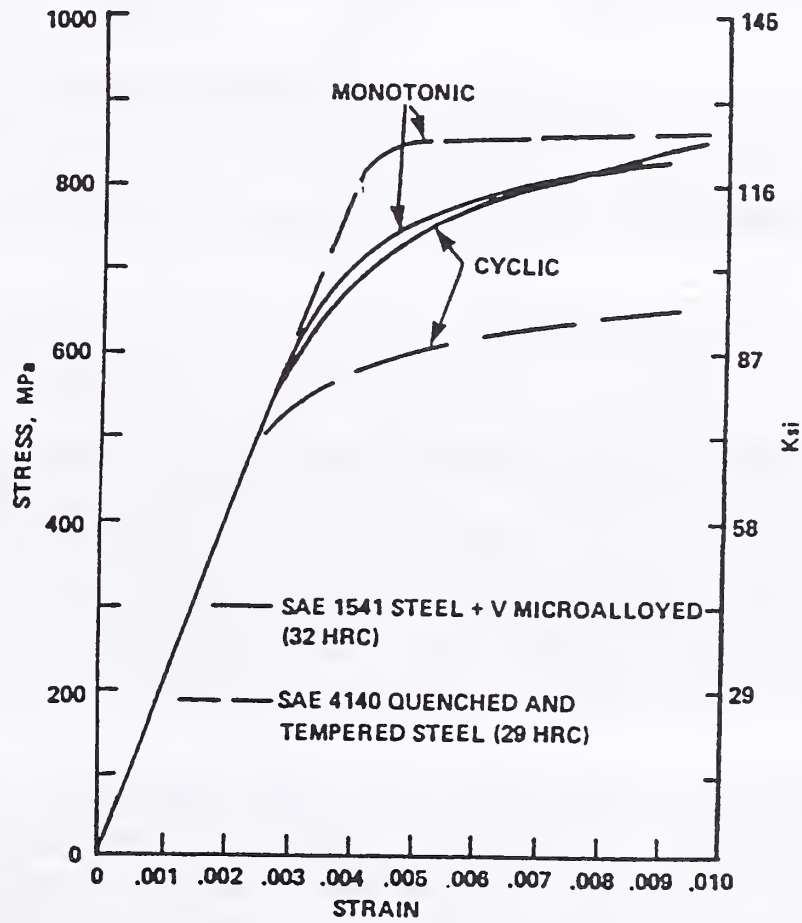


Fig. 20. A comparison of the stress-strain response of  $\alpha$ -P and Q&T steels (9).

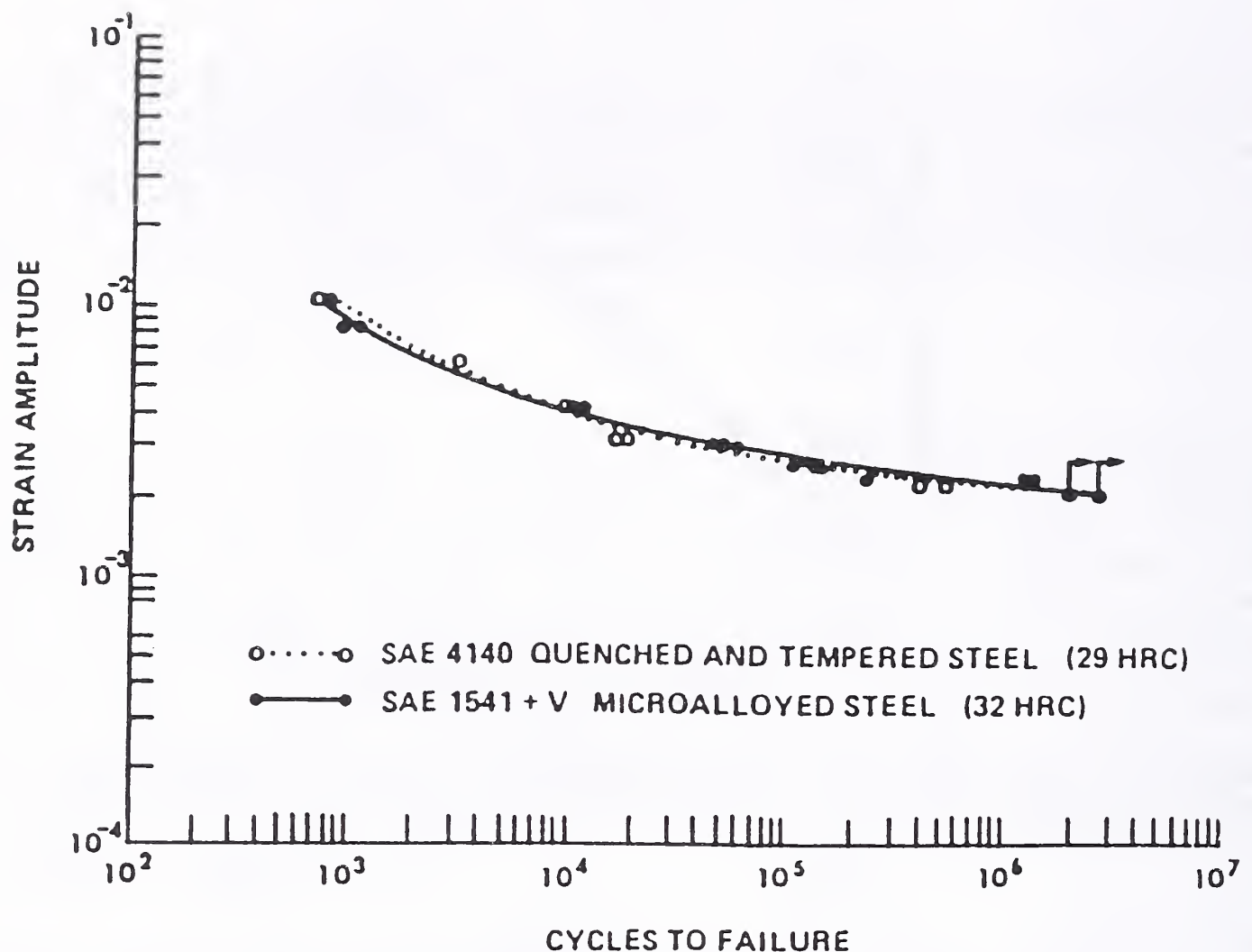


Fig. 21. A comparison of the strain-life fatigue curves of  $\alpha$ -P and Q&T steels (9).

### 1.5 Summary

The effect of different strengthening and toughening mechanisms on the YS and DBTT of steel is summarized in Fig. 22 (2). Grain refinement is the only strengthening mechanism that also improves DBTT. All other strengthening mechanisms reduce DBTT. The effects of strengthening mechanisms on other measures of toughness are not quantified in the literature. For instance, grain refinement has been known to decrease fracture toughness in Q&T AISI 4340 steel (44).

Lagneborg et al. (28) sum up the current state of alloy and processing design. The first goal is to maximize the strength, which is used to design a component, without sacrificing toughness, which generally determines the life of the component. Increasing the P content by raising the C content will raise strength, but decrease DBTT. It is possible to increase  $f(P)$  and keep the C content constant by decreasing the transformation temperature,

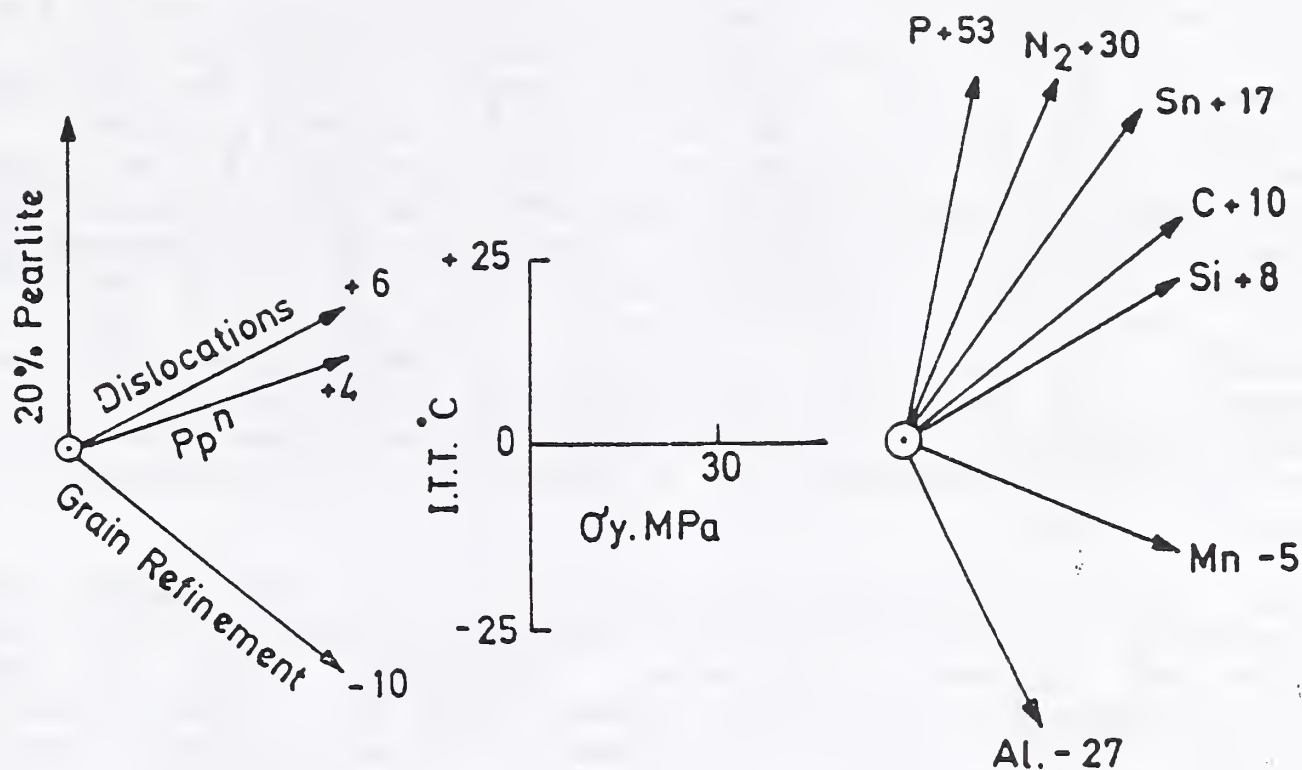


Fig. 22. Strengthening mechanisms and their effect on the DBTT (I.T.T.) in steels with a predominantly polygonal  $\alpha$  microstructure. Ratios indicate the change in DBTT for a 15 MPa increase in yield stress (2).

which is accomplished by increasing cooling rate and/or alloying. In this way, the maximum strength for a given C content is obtained. As the cooling rate and/or alloying increases at a constant C content,  $S_p$  decreases and a dilute P, one in which the  $Fe_3C$  platelet thickness is reduced, is formed.

Strengthening by the mechanism described above is limited by the formation of lower-temperature transformation products like bainite and martensite. The addition of V is an efficient way to add extra strength to  $\alpha$ -P steels, but again the higher strength comes with a lower toughness.

The final goal of alloy design is to maximize the impact toughness by minimizing the prior austenite grain size. Alloying with Al, Ti, and N and close control of the forging process can keep the prior austenite grain size relatively low. A problem arises because no one can specify exactly how much impact toughness is needed for a particular application.

The problem with low impact properties in  $\alpha$ -P steels is somewhat academic because fatigue is normally the limiting failure mode. In application, there is no design requirement for impact toughness. The high strain rate and notch used in CVN testing produces a highly constrained specimen for evaluation that is not typical for automotive applications. The CVN test is used frequently for many reasons. It is a well-accepted procedure around the world, it is inexpensive, and it has historical significance. The CVN test has been used since World War II for quality control purposes. It is extremely effective in identifying bad batches of low C and Q&T steels. However, impact properties are of no relevance in relation to the operating conditions for many automotive components and, therefore, the same criteria should not necessarily restrict the use of a new type of material, such as MA  $\alpha$ -P steel (22). These sentiments were repeated in private communications with several researchers who work for steel companies and steel users (45-47). It seems reasonable to conclude that impact properties are not of prime importance in components of this type, which normally fail by fatigue.

Overall,  $K_{Ic}$  or  $K_{Iv}$  testing appears superior to CVN testing because in fracture toughness testing, there is a direct link between results and fitness-for-purpose. Problems remain in applying fracture toughness testing on a wider scale for characterization of materials. First, there is the question of acceptance. Many steel users do not have the requisite expertise to apply fracture toughness technology. Another factor could be financial, although the use of short-rod testing would seem to minimize cost.

Characterization of fracture in tensile testing represents an opportunity to supplement our understanding of toughness. Tensile testing will have to be done in any case because tensile properties are the main issue. The additional effort required to characterize fracture in tensile testing is relatively small.

## 2. PROPOSED RESEARCH PROGRAM AT NIST

The program at NIST will address the research of structure-property relationships in four areas. The first part is to generate microstructures that are representative of thermo-mechanical processing on the material of interest. The second part is characterization of the pertinent structural features. The next phase of research addresses the determination of properties which are relevant to the potential applications for the material. The final part of the program integrates the research results into a model to predict properties from structure based on physical metallurgy principles.

Figure 23 shows a schematic diagram that is used to describe microstructural engineering research into TMP of steel. The end result of a study of structure-property relationships will be a

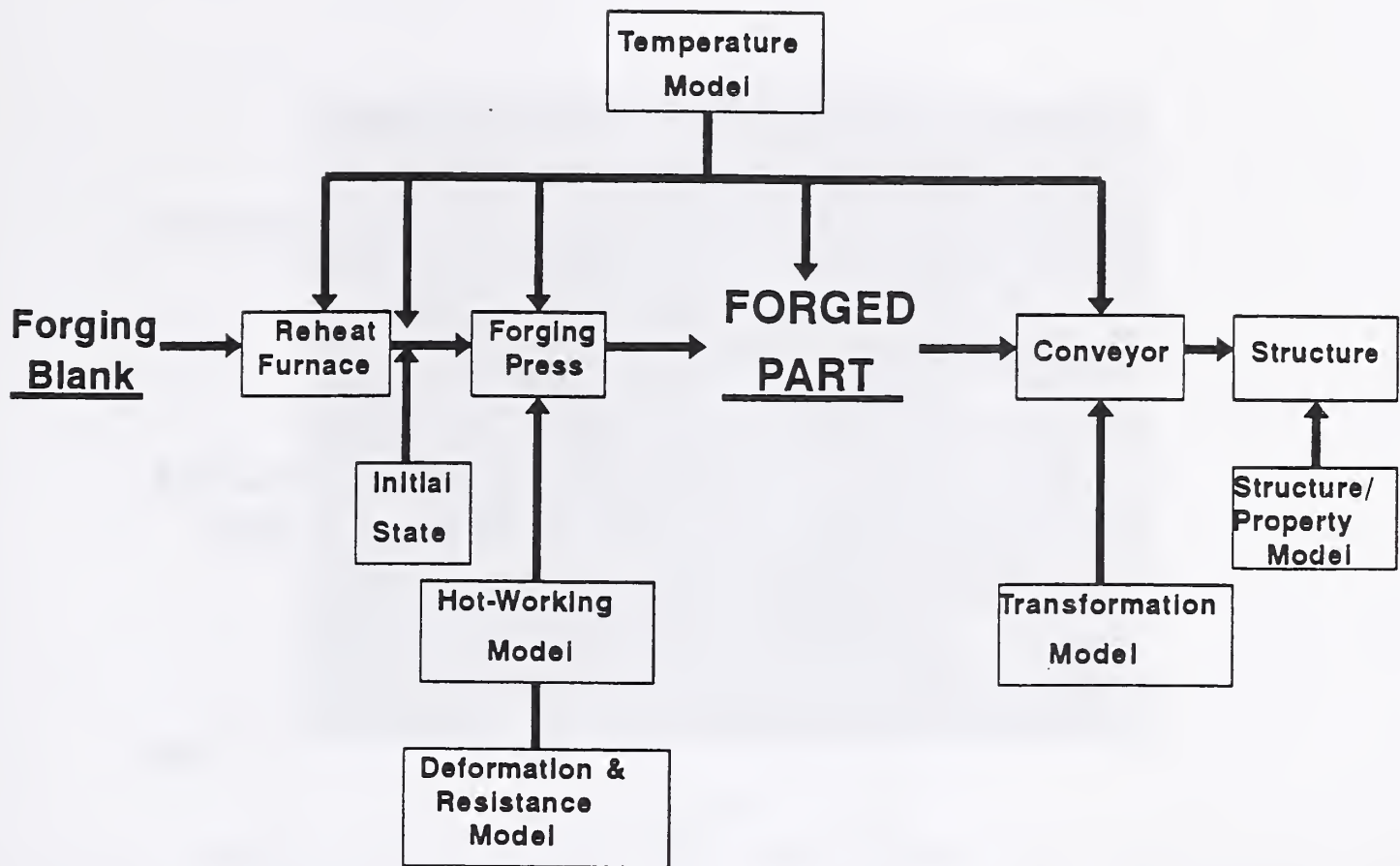


Fig. 23. Schematic diagram of TMP modeling showing the relationship between the structure-properties modeling and other efforts.

quantitative procedure that will take the significant structural factors (output of transformation model) as input values and predict their effect on properties, as related to performance as much as possible. The ultimate goal is to be able to predict the processing variables that will produce acceptable performance. In the case described here for forging steels, the end product of microstructural engineering will be a set of processing conditions that will provide the desired fatigue life.

## 2.1 Generation of Representative Microstructures

A high-strain-rate servo-hydraulic mechanical test system with a 500 kN load capacity has been designed to simulate forging, typically used in manufacturing of automotive parts and other semi-finished bar products. Average plastic strain rates of about 10 to 15 per second are possible. A schematic diagram is shown in Fig. 24 to illustrate the loading apparatus to be used in the initial testing. The specimens are solution heat treated in a convection box furnace, using no special atmospherical control, and then placed in the load frame. The hot specimen is supported on the

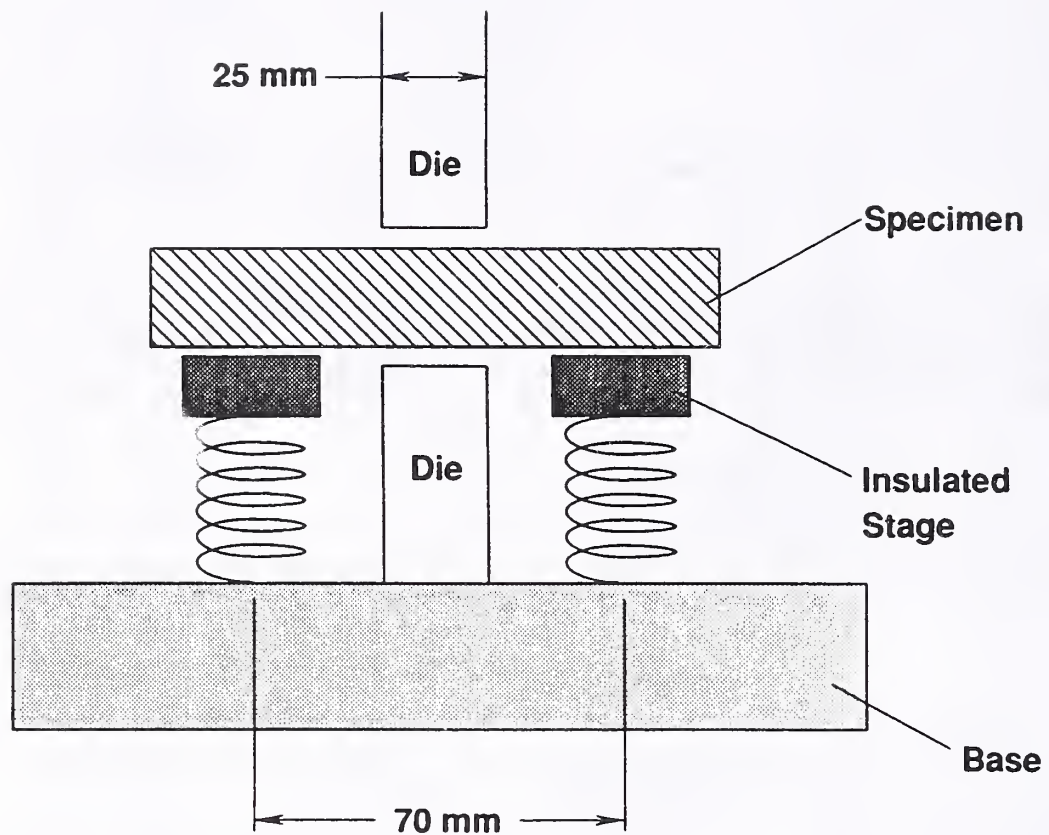


Fig. 24. Schematic diagram of loading fixture for large TMP simulator.

ends by spring-loaded, insulated columns. The specimen is then given a prescribed deformation with a known strain rate. An example of the load vs. stroke data for one experiment is shown in Fig. 25. A sheet of graphite, 0.25 mm thick, is used between the specimen and the dies to minimize friction during deformation.

Experimental variables that are important in generation of the representative microstructures for the initial survey of properties are:

- (1) reheating temperature before forging,
- (2) strain during forging,
- (3) cooling rate from forging temperature, and
- (4) alloy composition.

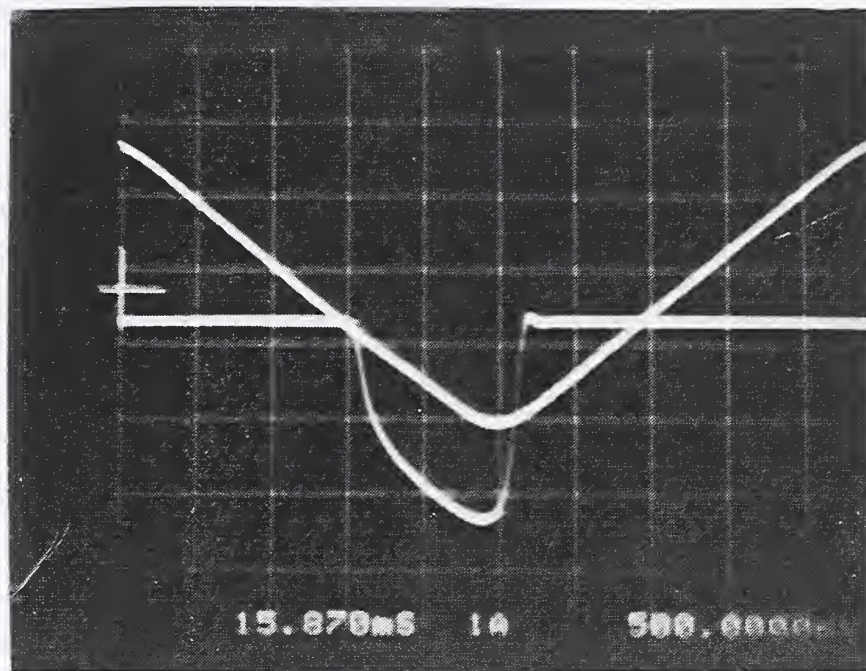


Fig. 25. Load (vertical axis for the bottom line on the figure) and stroke (vertical axis for the top line on the figure) plotted against time (horizontal axis for both curves) data taken from TMP experiment on SAE 1141 steel.

Figure 26 shows a schematic diagram that illustrates the thermomechanical variables to be used in the first series of tests. The initial reheat temperature will be either 950, 1100, or 1215°C. Typically, the reheat temperature for forging is 1200 to 1300°C, allowing V and Nb to dissolve in the austenitic matrix. After reheating, the specimens will be furnace-cooled to either 1100 or 950°C before deformation so that the finish-forging temperature is close to 1100 or 950°C, respectively. The deformation associated with forging is usually finished with minimal heat losses (finish-forging temperature >1100°C), making plastic flow easier by reducing the loads required for forging and minimizing die wear. Some forging shops are working with lower reheat and finish-forging temperatures in order to save on energy costs and to limit decarburization that must be machined off later.

A high and a low degree of deformation ( $\epsilon$  of about 0.5 and 0.2, respectively) will be done for selected conditions. After deformation, specimens will be cooled to RT at different rates, so that the effect of cooling different section sizes in still air can be evaluated.

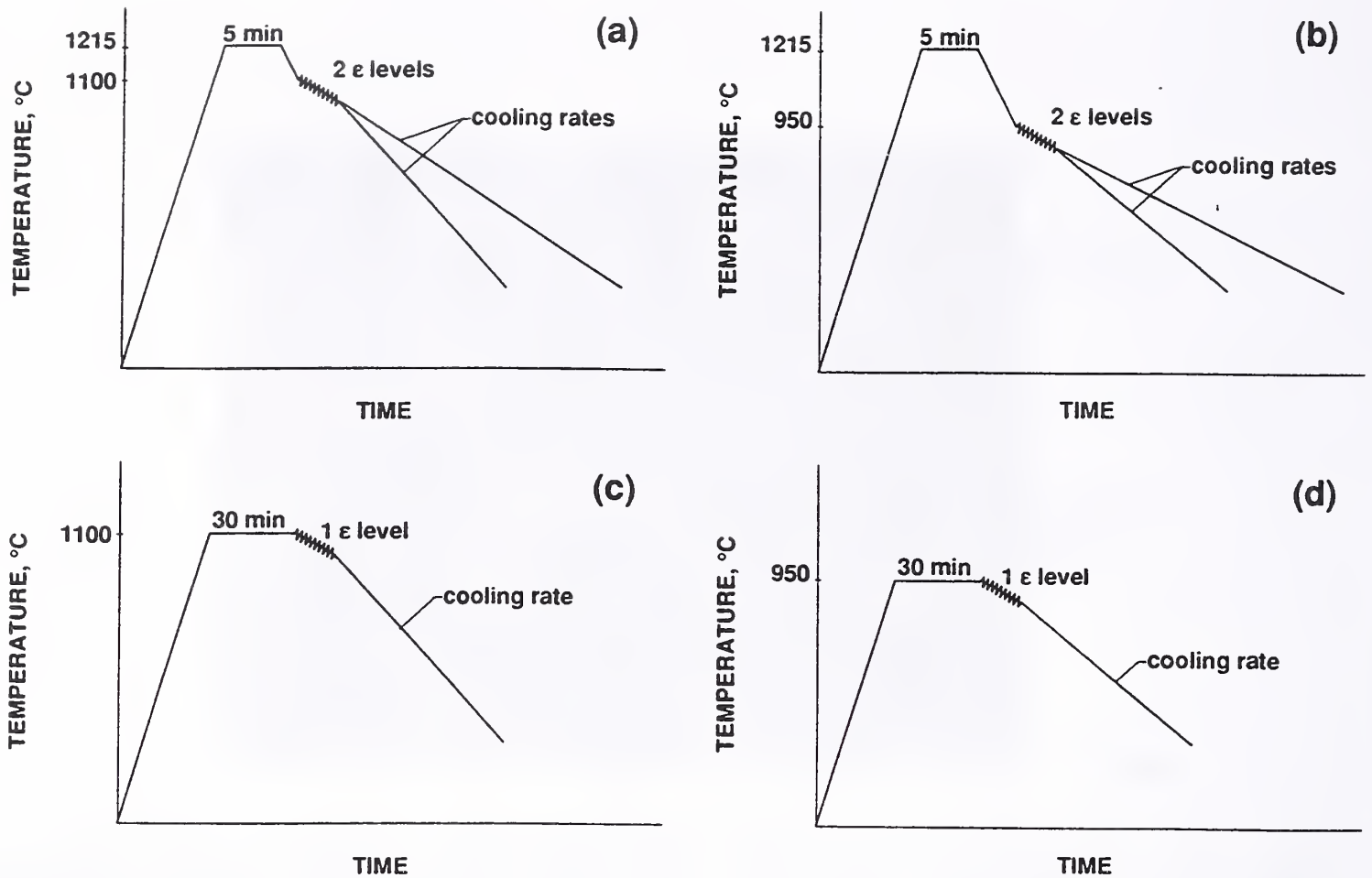


Fig. 26. Schematic diagram showing the four different TMP schedules to be evaluated in the initial study.

For the initial phase of our experimental program, we will use two different alloys, SAE 1141-V and -Nb. The composition of the alloys is shown in Table 2. Both are classified as free-machining grades due to the high S content. The main difference between the two steels is the MA additions of V in one case and Nb in the second. Within the next year, we expect to obtain additional steels with slightly different alloying additions so that the effects of the high S content and MA can be studied further.

Table 2. Chemical composition (mass %) of steels for test program.

C	Mn	P	S	Si	Cr	N	MA element
0.37	1.44	0.012	0.100	0.25	0.08	0.009	0.07 V
0.42	1.58	0.013	0.100	0.25	0.09	0.009	0.026 Nb

## 2.2 Characterization of Structure

The characterization will include standard metallographic procedures for light and electron microscopes. For the study of MA  $\alpha$ -P steel, the relevant features to be measured include  $f(\alpha)$ ,  $S_p$ ,  $\alpha$  grain size,  $p$ ,  $D$ ,  $f(\text{ppt})$ , and  $x_{\text{ppt}}$ . For the initial survey of properties, transmission electron microscopy (TEM) examination is not feasible for every processing condition, but can be evaluated later for selected conditions. In addition to microstructural features, it could be important to document the microhardness (DPH) of each phase ( $\alpha$  and P) where possible. DPH could be valuable for two reasons. First, where  $S_p$  varies and is discontinuous, DPH could give a direct estimate of the strength of the P phase without measuring  $S_p$ .

The characterization of the P colonies is important for several reasons. First,  $f(P)$  is a big contributor to the strength and is related to different factors such as  $S_p$ ,  $t$ , and  $p$ . The scale of the features is small,  $S_p$  can be as fine as 65 nm (48). TEM studies may be required to accurately describe the features of P. Thermal analysis of the cooling curves after processing could help characterize the features because  $S_p$  is mainly a function of the temperature for transformation (49).

Additional study of selected broken specimens will be done to document the fracture mechanisms. SEM observation of fracture surfaces and polished sections through failed specimens can be used to associate damage mechanisms to microstructural features (this part has received little attention in the literature).

## 2.3 Determination of Properties

Standard tension testing of cylindrical specimens and hardness testing (Rockwell C or B scale) will be the standard procedure for experimental evaluation of strength. In the initial survey of properties, %RA and the stresses at fracture will be used as measures of toughness. The procedure for calculating  $\sigma_o$  and  $\sigma_T$  are found in Appendix A. For selected processing conditions, chevron-notch fracture toughness tests at RT, CVN transition curves, and possibly fatigue testing can be included for a more complete evaluation of toughness.

Machinability is also an important consideration in the choice of material for many applications (4,13). Typically, the evaluation of machinability is determined by measurement of tool life during different operations like milling, turning, and hole drilling, requiring a large volume of material which is not available in a small-scale simulation. Machinability is generally assumed to be a function of hardness, a lower hardness is easier to machine. In practice, there is a range of hardness specified for a given application so that the material will be strong enough to withstand the loading during application, but soft enough to be machined.

Empirical correlations between hardness and machinability, and hardness and tensile properties are used to predict performance.

## 2.4 Integration of Structure and Properties for Modeling the Application

The prediction of mechanical properties from structural features is the goal of our research. Considering the prediction for YS and UTS of  $\alpha$ -P steels, the existing equations from Gladman and Pickering (18) are adequate to evaluate strength. For the precipitation strengthening contribution, Eq. (2) is the best way to quantify the effect; it is well supported by theory and limited experimental evidence, but requires extensive TEM observations for application. Simpler experimental procedures for the characterization of fine-scale precipitation would be extremely helpful in this regard.

For the prediction of toughness, tensile fracture characterization is key. A test procedure to evaluate toughness other than CVN testing, particularly one that includes a fitness-for-service analysis, could aid significantly in application of MA  $\alpha$ -P steels to a wider range of use. By characterization of the stresses at fracture and calculation of  $\sigma_c$  for the initiation of voids, toughness is related to the physical process of ductile fracture and distinct microstructural features. The interpretation of  $\sigma_c$  for void nucleation from microstructural features is new and the relevance is open to debate. However, the procedure for the characterization of the stresses at fracture is simple and easily applied. Correlations of  $\sigma_c$  vs.  $K_{IV}$  and  $\sigma_c$  vs. fatigue life could be studied and would provide a basis for evaluation of the tensile fracture characterization.

## 3. PRELIMINARY STUDY

### 3.1 Introduction

In this part of the report, we will show preliminary results from our initial study on the thermomechanical processing (TMP) of MA  $\alpha$ -P steel. The goals for this study are as follows: (1) to illustrate the facilities that are available at NIST for the study of the TMP of steel, (2) to compare the results of the larger simulator to previous results from earlier work done here at NIST on smaller specimens, and (3) to evaluate the existing equations that predict properties from microstructure.

### 3.2 Material and Experimental Procedures

The composition of the steel used in this preliminary work, shown in Table 3, is similar to SAE 1141 with a Nb addition. This alloy has been used in several recent studies by Cheng and co-workers

(25,50,51). The material was received in the form of a 30-mm-diameter bar, and the hardness was about  $R_c$  18.

Table 3. Chemical composition of SAE 1141 with Nb (mass %).

C	Mn	P	S	Si	Cu	Ni	Cr	Mo	N	Nb
0.42	1.49	0.015	0.099	0.26	0.16	0.06	0.06	0.009	0.0075	0.039

The microstructure of the as-received bar in the transverse orientation is shown in Fig. 27. The pearlitic phase occupies most of the area while the  $\alpha$  phase, 5 to 8% of the area, is present as a network at the prior austenite grain boundaries. The prior austenite grains vary in size, but the average diameter is about 40  $\mu\text{m}$ . Part of the reason for the variation in prior austenite grain size could be the nonuniform distribution of MnS particles in the structure. At the highest magnification (Fig. 27b), spacing of carbide platelettes in the pearlitic phase can be observed with the light microscope in some areas. The finest spacings could only be observed in SEM. The minimum  $S_p$  observed was about 0.15  $\mu\text{m}$ . The true spacing should be equal to the finest observable spacing.

In Fig. 28, the MnS inclusions are shown in longitudinal and transverse sections. In the transverse section, Fig. 28a, the particles are largely spherical and located in the  $\alpha$  network that formed at the prior austenite grain boundaries. The particles appear to have pinned the austenite grains during processing, preventing grain growth, as suggested by others (13). When viewed in the longitudinal section, Fig. 28b, the inclusions are strung out along the rolling direction.

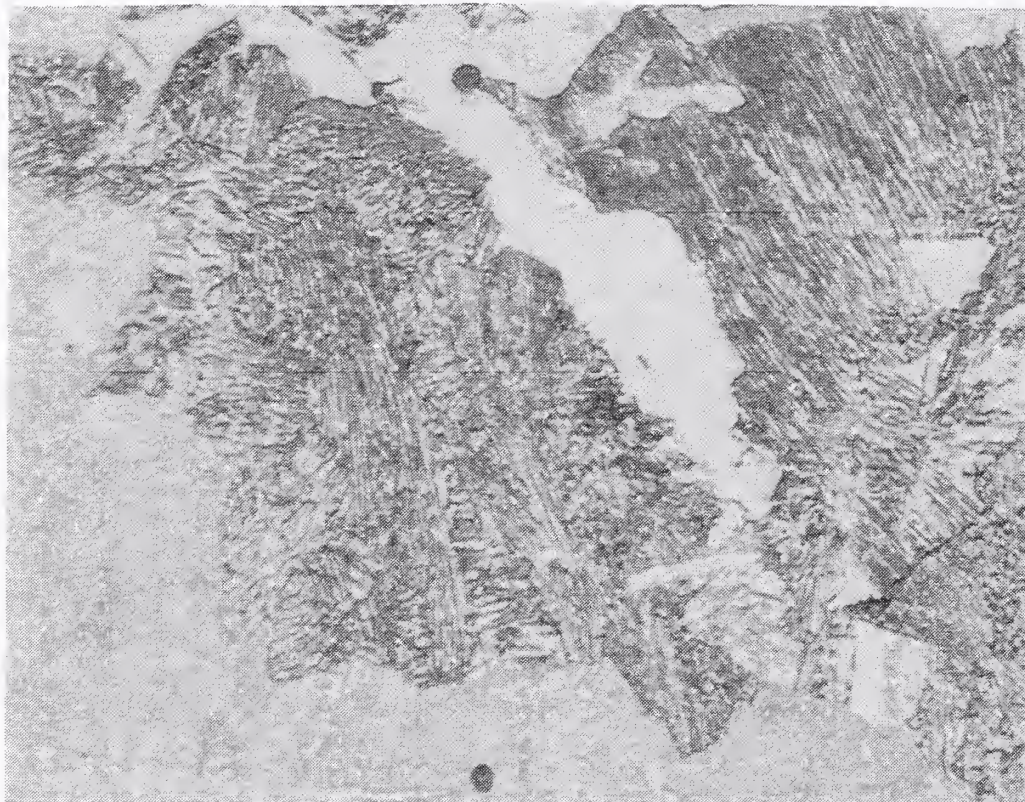
Mechanical tests were conducted on the as-received material as well as the processed steel so that the effect of subsequent TMP could be quantified. Hardness testing was done on the Rockwell C scale ( $R_c$ ) to determine the bulk hardness, and on the Vickers scale (DPH) with 100 and 10 g loads to determine the micro-hardness. The size of indentation in the DPH test is an important consideration. For the 10 g load, the indentation is correspondingly small, but the scatter in results may increase as the load decreases. The 100 g load should produce more uniform results, but is less discriminating with regard to the individual microstructural features, particularly, the hardness of  $\alpha$  in a thin network may be difficult to characterize.

Tensile and CVN specimens were oriented along the rolling direction of the bars. The tensile specimens were cylindrical in shape with a 6.4 mm diameter and a 25 mm long gage section. The crosshead rate for tension testing was 0.5 mm/min. In addition to the typical tensile properties that are reported, values for  $\sigma_0$



(a)

50  $\mu\text{m}$



(b)

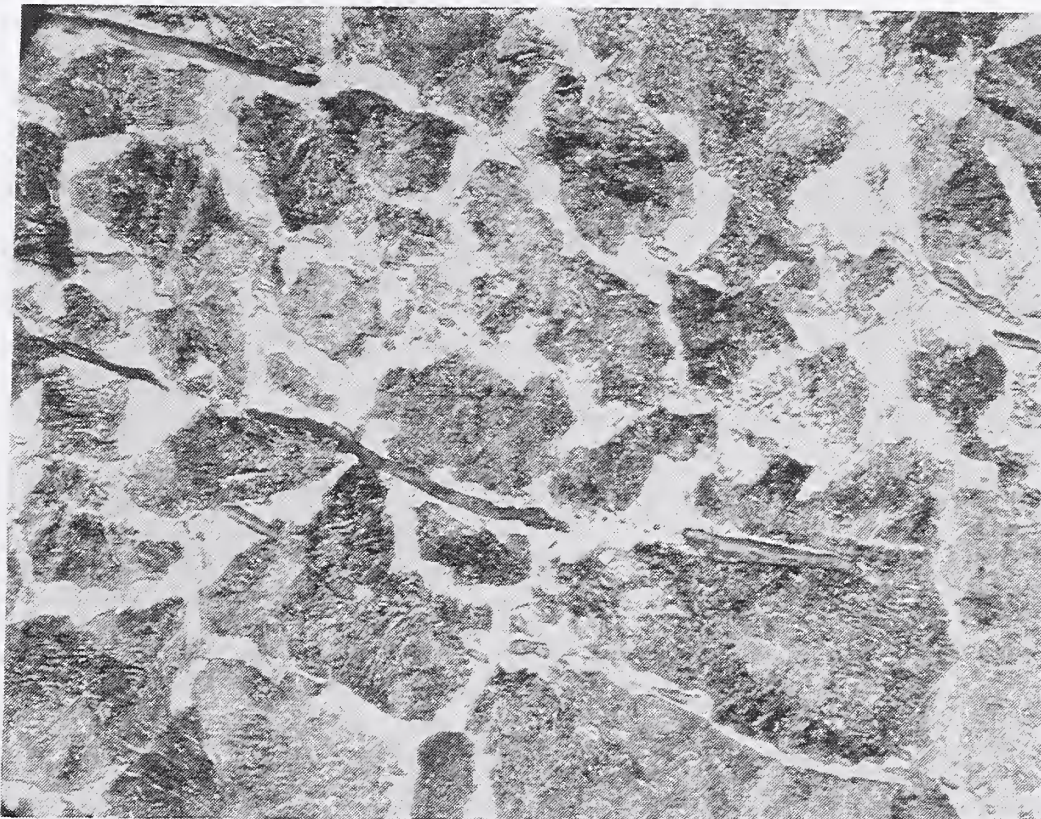
5  $\mu\text{m}$

Fig. 27. As-received microstructure of SAE 1141-Nb steel (a) low magnification, (b) high magnification.



(a)

12  $\mu\text{m}$   

(b)

12  $\mu\text{m}$   


Fig. 28. Appearance of MnS particles in microstructure:  
(a) transverse section and (b) longitudinal section.

(equivalent plastic flow stress at fracture) and  $\sigma_c$  (critical stress for void nucleation at fracture) (42) are described in Appendix A. CVN specimens were machined according to ASTM E 23, type A.

Specimens were processed in TMP simulator described earlier. The specimens were deformed to a true strain of about 0.8 at an average strain rate of 15. The temperature variables in the experiments are listed in Table 4.

Table 4. Temperature variables used in preliminary study.

Spec.	Reheat Temperature	Deformation Temperature	Cooling Rate <sup>+</sup>
D1	*	*	*
D2	900°C	900°C	0.8°C/s
D3	1100°C	1100°C	0.9°C/s

<sup>+</sup> Cooling rate is defined by the time to cool from 750 to 500°C.

\* As-received condition.

### 3.3 Results

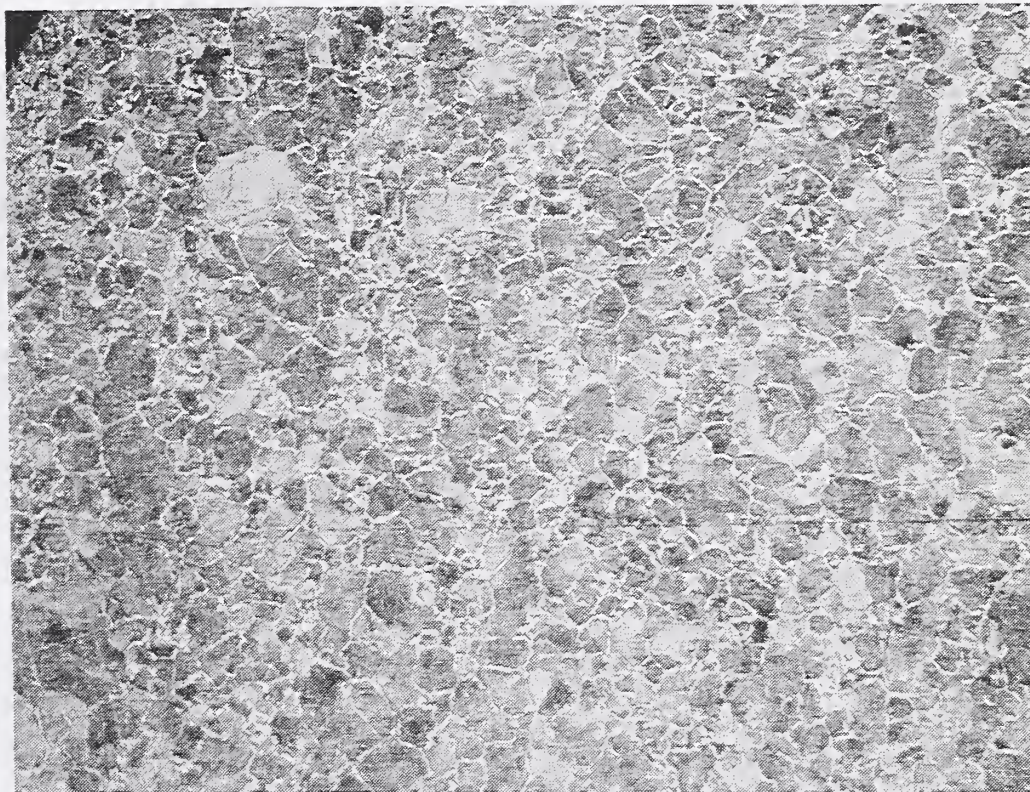
#### 3.3.1 Microstructure

The microstructures generated during TMP are shown in Figs. 29 and 30. For the D2 condition (900°C deformation, shown in Fig. 29), the  $\alpha$ -P features are much finer than that of D1 (as-received). The  $\alpha$  phase occupies between 35 and 43% of the cross sectional area. The  $\alpha$  grain size is about 5  $\mu\text{m}$  while p is slightly larger, about 10  $\mu\text{m}$  average diameter.  $S_p$  for D2 is variable, but in general appears finer than that found in D1, about 0.13  $\mu\text{m}$ .

For the higher processing temperature (1100°C, condition D3), the microstructure shown in Fig. 30 is similar to that of D1 (as-received), but refined slightly. The prior austenite grain size is about 20  $\mu\text{m}$ , and the  $\alpha$  content is about 8 to 10% of the area. The value of  $S_p$  for D3 is similar to that for D1, about 0.15  $\mu\text{m}$ .

#### 3.3.2 Mechanical Properties

The mechanical properties at RT are summarized in Tables 5 and 6. The tensile properties do not change significantly with the different processing conditions. The CVN test results are interesting because condition D2 failed by a fully ductile mode. The energy absorbed in testing D2 was about 50% higher than the



(a)

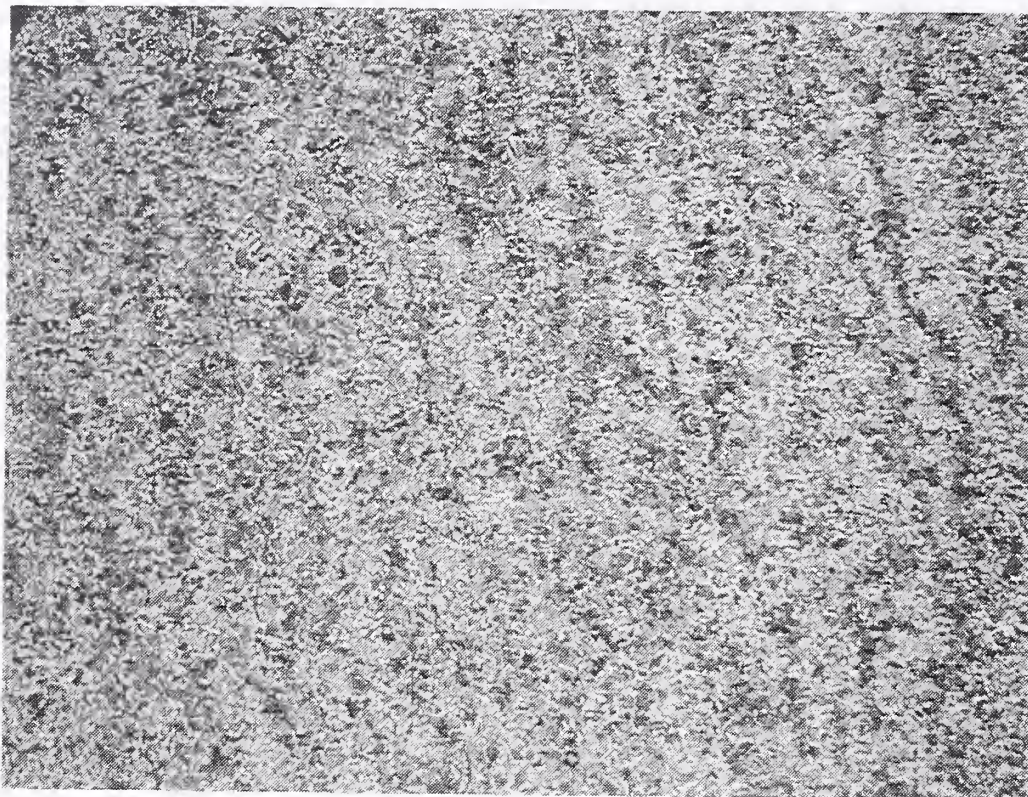
50  $\mu\text{m}$



(b)

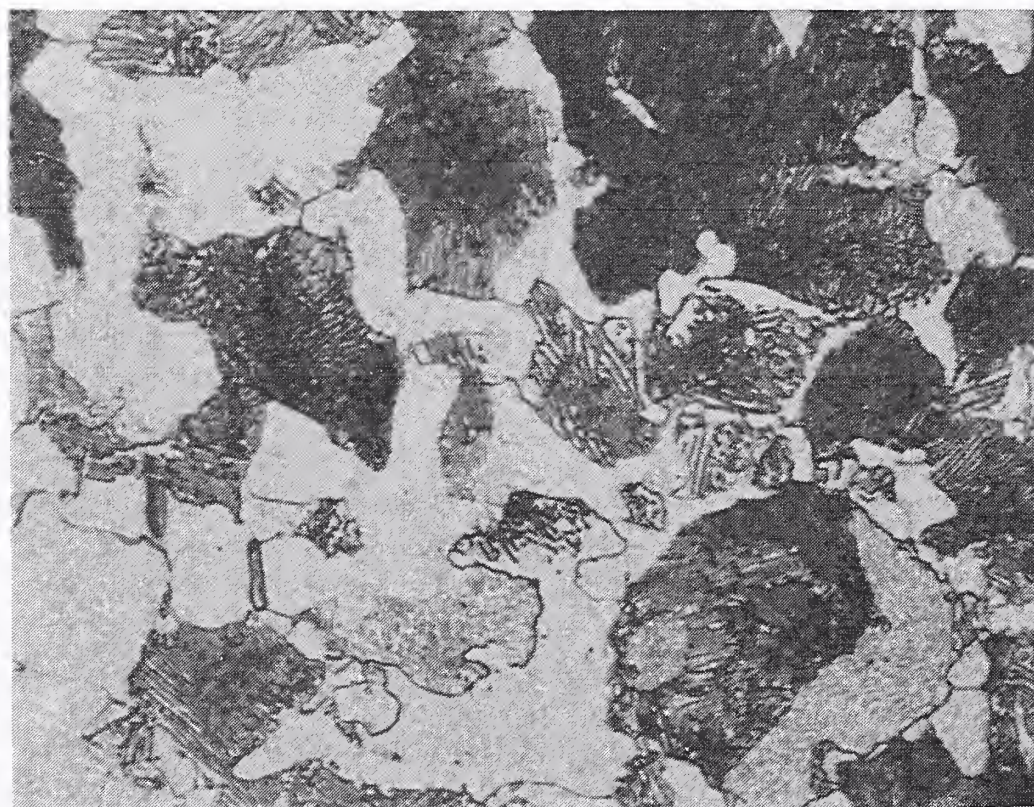
5  $\mu\text{m}$

Fig. 29. Microstructure of SAE 1141-Nb steel after deformation at 1100°C and air-cooling (a) low magnification, (b) low magnification.



(a)

50  $\mu\text{m}$



(b)

5  $\mu\text{m}$



Fig. 30. Microstructure of SAE 1141-Nb steel after deformation at 900°C and air-cooling (a) low magnification, (b) high magnification.

average for conditions D1 and D3, where the failure mode was a mixed ductile-brittle one. The properties are typical of a  $\alpha$ -P steel (compare the data for 1141-Nb with that shown in Fig. 2).

The hardness testing is summarized in Table 7. Given the size of the indentation and the thin network of  $\alpha$ , DPH of  $\alpha$  could not be determined in some cases. The hardnesses of D1 and D3 are similar, as were the microstructures and mechanical properties. The bulk hardness for condition D2 is lower than the others. For the pearlitic phase, the lower DPH for the 100 g load is probably due to the soft, ferritic matrix that surrounds the relatively small P colonies. With the lighter load, the pearlitic phase in condition D2 has the highest DPH because the indentation is small enough to only sample P, and not the ferritic phase. The average microhardness for  $\alpha$  and P is always higher than the average bulk hardness. The scatter in DPH testing is greater for the lighter load.

Table 5. Tensile test results at RT on SAE 1141-Nb steel.

Specimen #	YS, MPa	UTS, MPa	% Elong.	% RA
D1-1	475	760	15.6	30.0
D1-2	467	748	15.1	29.3
D2	486	703	19.2	32.5
D3	493	774	16.3	30.0

Table 6. CVN test results at RT on SAE 1141-Nb steel.

Specimen #	% Cleavage Fracture	Absorbed Energy, J
D1-1	48	33.5
D1-2	48	22.2
D1-3	42	37.3
D1-4	50	26.0
D2	0	43.4
D3	38	25.2

Table 7. Summary of hardness testing.

Process Condition	Brinell -- bulk	DPH, 100 g load	DPH, 10 g load
D1 -- $\alpha$	221, 217, 217 214, 215 ave. = 217	-----	-----
D1 -- P		269,266,290,265,275 ave. = 273 (Brinell 264)	290,237,254,279,263 ave. = 265 (Brinell 253)
D2 -- $\alpha$	203, 202, 202, 202, 203 ave. = 203	-----	221,279,214,219,260 ave. = 239 (Brinell )
D2 -- P		212,224,227,243,226 ave. = 226 (Brinell 219)	279,286,293,313,325 ave. = 299 (Brinell 286)
D3 -- $\alpha$	221, 222, 222, 224, 222 ave. = 222	-----	297,263,226,219,260 ave. = 253 (Brinell 243)
D3 -- P		258,252,264,262,243 ave. = 256 (Brinell 243)	245,297,263,297,272 ave. = 275 (Brinell 264)

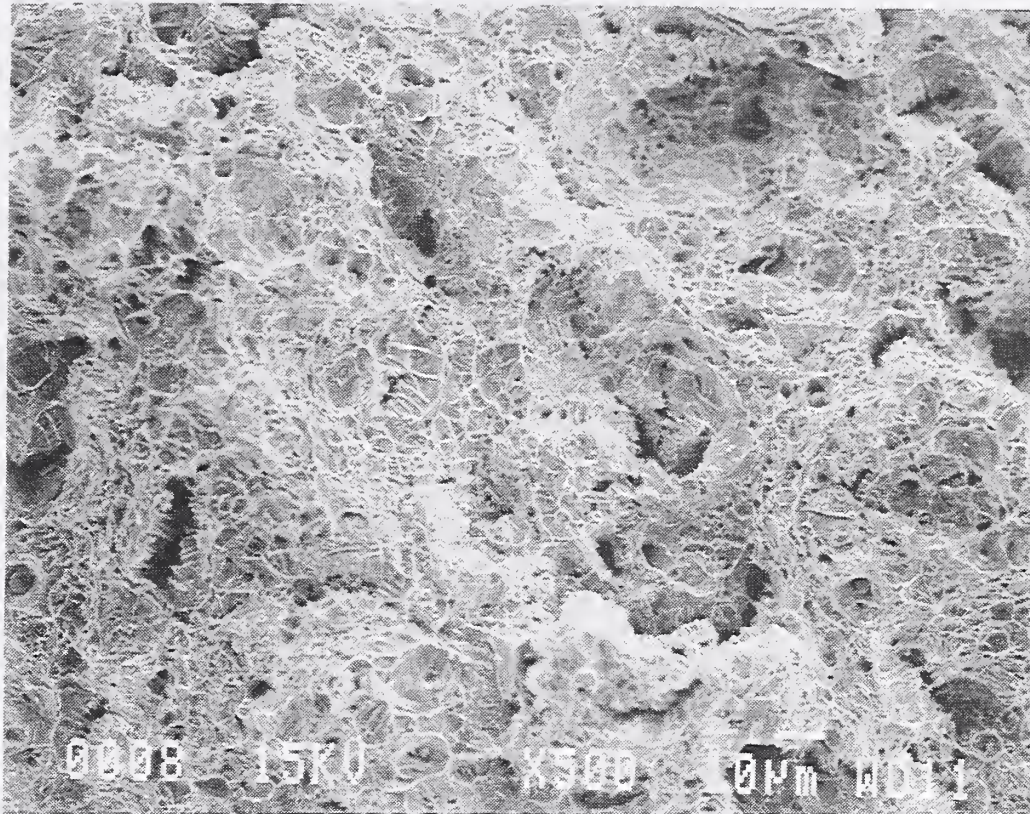
The tensile fracture stresses are shown in Table 8. These stresses, along with the %RA, characterize the ductile fracture behavior of the material. The critical stress is essentially constant for the three different processing conditions. Equation 12 can be used to predict the effect of changes in the microstructure on % RA. For condition D1, the predicted % RA would be 32%, agreeing well with the measured value of 30%. However, for condition D2, the prediction, 47%, is considerably higher than the measured value, 33%.

Table 8. Tensile fracture stresses (MPa).

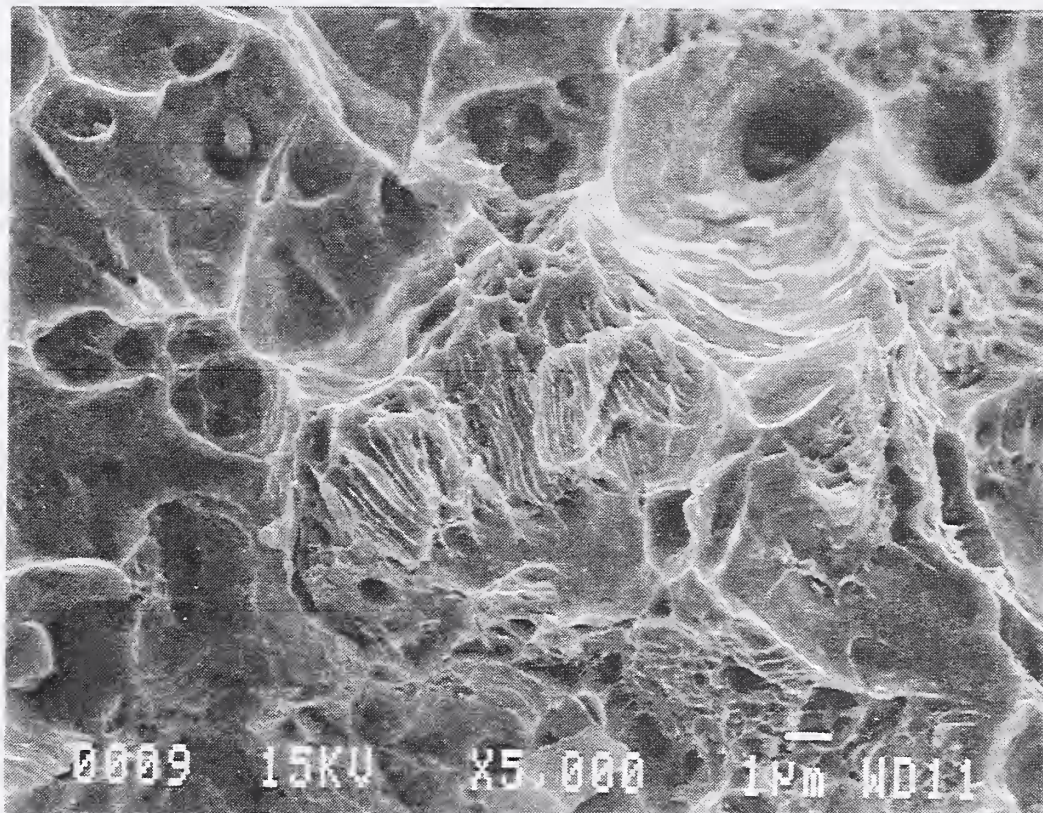
Specimen #	$\sigma_o$	$\sigma_T$	$\sigma_c$
D1-1	1072	770	1842
D1-2	1026	727	1753
D2	1129	686	1815
D3	1076	751	1827

### 3.3.3 Fractography

The appearance of the tensile specimens from all three conditions was similar. The fracture surface from an as-received tensile specimen is shown in Fig. 31. At 500x, a few irregular troughs



(a)



(b)

Fig. 31. Fracture surface of tensile specimen taken from as-received steel (a) low magnification, (b) high magnification.

and ridges, 50 to 100  $\mu\text{m}$  in size are visible. At higher magnification, dimples associated with inclusion particles (labeled A) are the dominant features on the surface, but smaller facets (labeled B) are found between patches of dimples. The small facets are areas where the fracture went through a pearlite colony.

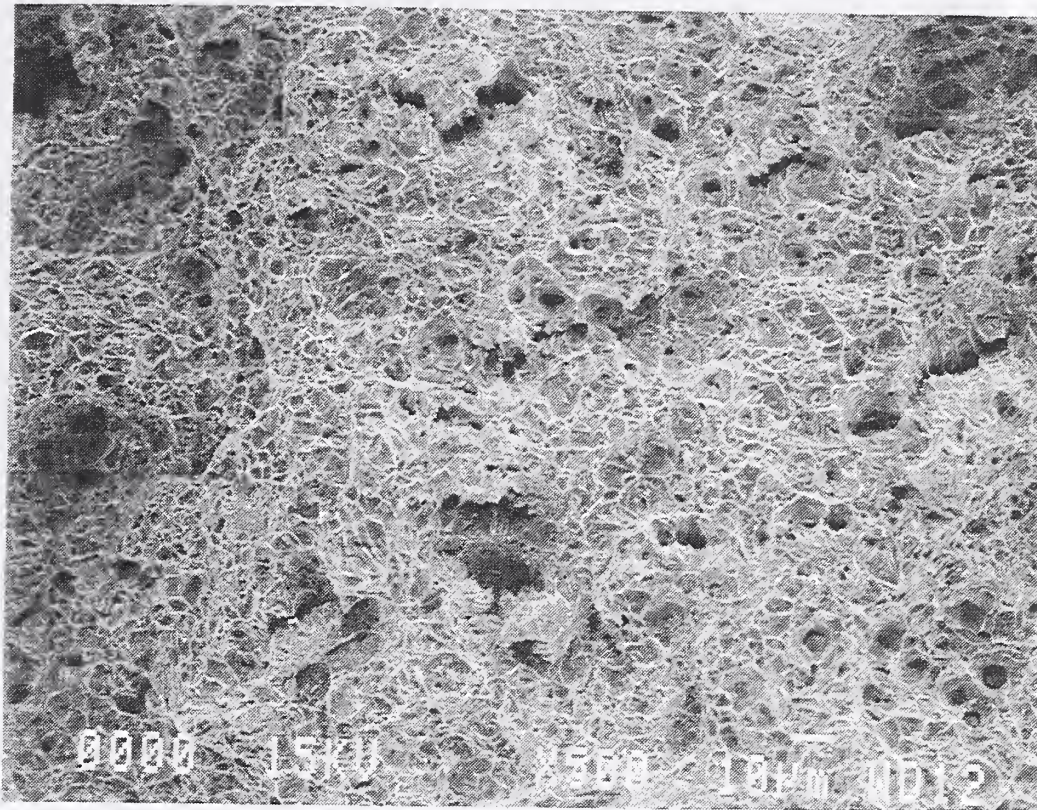
For condition D2 (processed at 900°C), the tensile fracture surface is shown in Fig. 32. The higher  $\alpha$  content in the microstructure has little influence on the appearance. The dominant features are inclusion-nucleated dimples. Patches of submicrometer-sized facets are found on the surface between the larger dimples. The consistent tensile fracture appearance can be related to the similar fracture stresses of the tensile specimens.

The appearance of CVN fracture surfaces is different from that of the tensile specimens. For conditions D1 and D3, large areas of cleavage fracture are found on the surface (see Table 6). For condition D2, no cleavage is observed on the fracture surface, but the features are still different from that observed on the tensile fracture surface. Figure 33 shows a representative area from the region directly ahead of the notch tip where the fracture process started. Numerous dark cavities, 10 to 50  $\mu\text{m}$  in size, are prominent on the surface between the other fracture surface features. The cavities are smaller, 5 to 10  $\mu\text{m}$ , than those on the tensile fracture surface in Fig. 32. Otherwise, the fracture surfaces of the tensile and CVN specimens are similar.

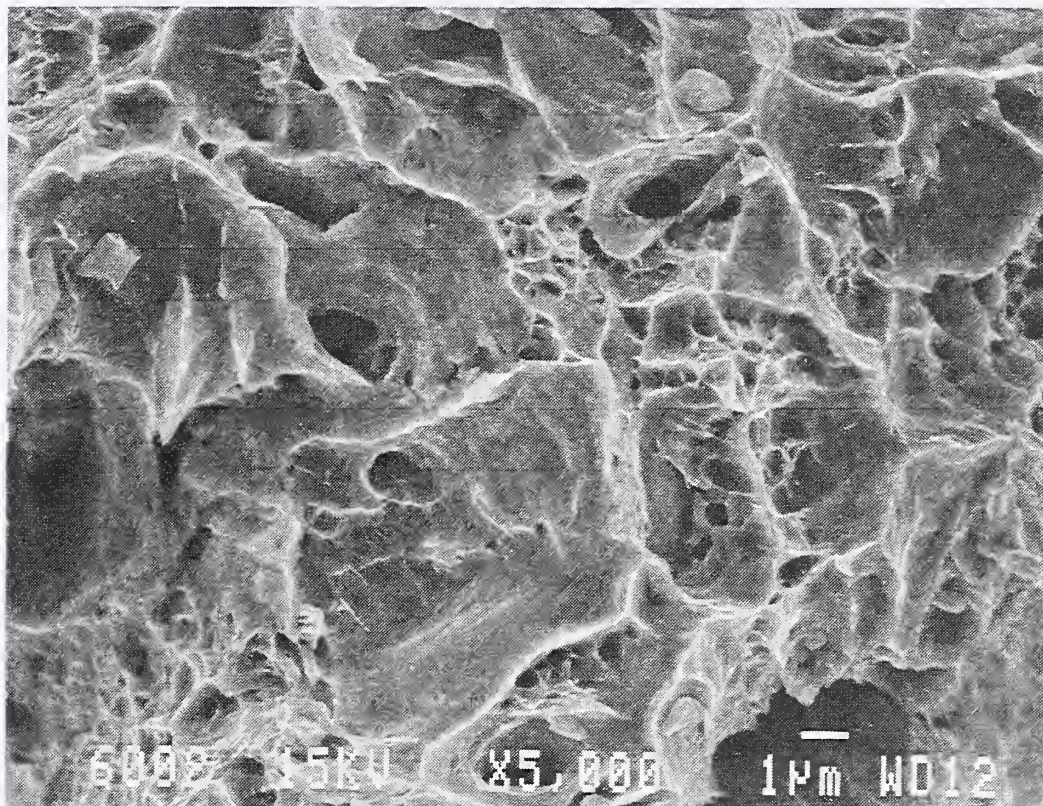
### 3.4 Discussion

The three different processing conditions considered in this preliminary study have altered the microstructure; however, the measured tensile properties are only slightly affected by the change in features, the biggest difference is in YS between D1 and D3, about 10%. CVN energy absorbed at RT does significantly increase for the finest ferrite grain size (condition D2).

There are considerable microstructural differences between conditions D1 and D2. The  $\alpha$  content increases from about 5 to 40% of the volume, and  $S_p$  decreases from 0.15 to 0.13  $\mu\text{m}$ . The  $\alpha$  grain size for condition D1 is taken as the thickness of the grain-boundary network, about 3  $\mu\text{m}$ , while the  $\alpha$  grain size is about 5  $\mu\text{m}$  for condition D2. It is helpful to consider the changes in microstructure and their effect on tensile properties, related to Eqs. (7) and (9). Kirby et al. (36) used these same types of equations and found excellent agreement between the measured tensile properties of a  $\alpha$ -P steel which was not precipitation strengthened and predicted values. For V-containing steels, the equations underpredicted the strengths.



(a)



(b)

Fig. 32. Fracture surface of tensile specimen taken from steel deformed at 900°C and air-cooled (a) low magnification, (b) high magnification.

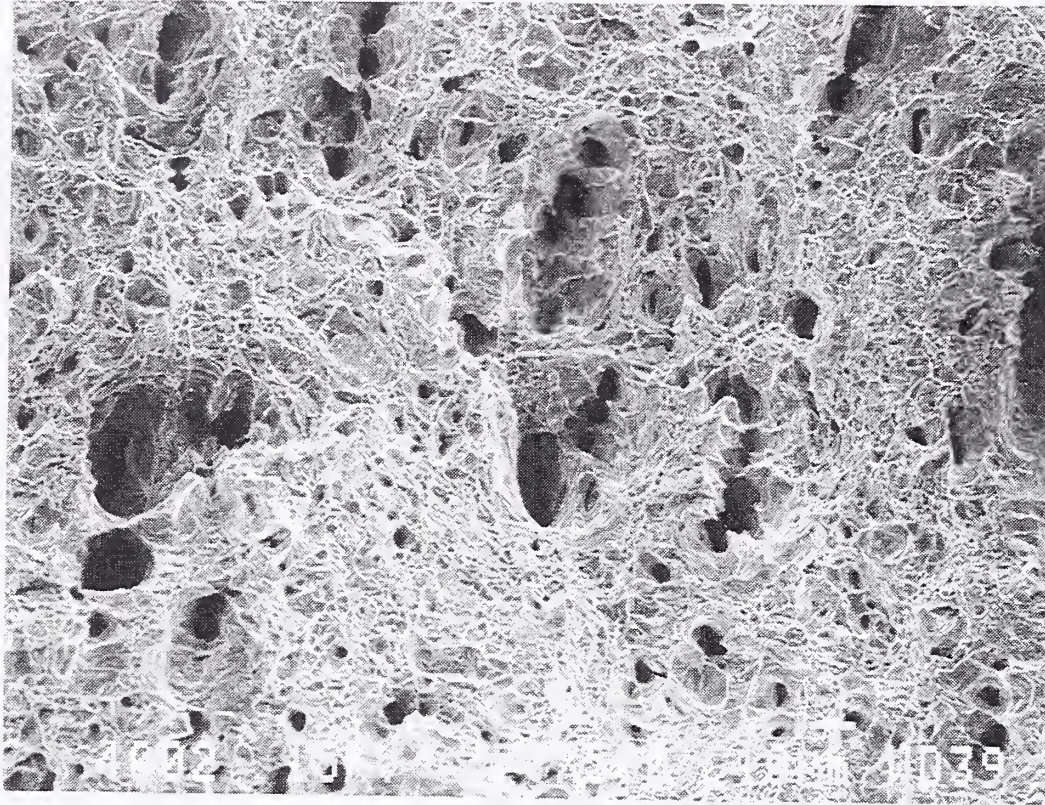


Fig. 33. Fracture surface of CVN specimen taken from steel deformed at 900°C and air-cooled.

Table 9 compares the predicted values for YS and UTS from Eqs. (7) and (9) for conditions D1 and D2 with measured values from Table 5. The predictions are 10 to 15% off the measured values, overpredicting the properties for D1, and underpredicting YS and UTS for D2. In this case, the under prediction is not related to precipitation strengthening because the Nb-treated steel used in this study does not contain any V.

Table 9. Comparison between measured and predicted tensile properties for SAE 1141-Nb steel.

Condition	Eq. (7) YS, MPa	Measured YS, MPa	Eq. (9) UTS, MPa	Measured UTS, MPa
D1	521	471	848	754
D2	405	486	641	703

One possible reason for the problem in predicting strength is the characterization of the pearlitic phase. The measurements of  $S_p$  and  $f(P)$  are probably not sufficient for two reasons. First, the

pearlitic phase of the Nb-treated steel used in this initial study has a discontinuous carbide morphology in many regions. Figure 34 shows a typical region where there are numerous P colonies along with the ferrite network and MnS particles. The carbide constituents in the pearlitic phase do not always form the classical fingerprint pattern that can be characterized by a single parameter,  $S_p$ . The second factor is that the dilution of P depends upon the processing conditions. For condition D1 and D3, where there is little proeutectoid  $\alpha$ , the dilution is high. For condition D2, where the  $\alpha$  content is much higher, the dilution is relatively low. Additional work is needed to improve the characterization of the pearlitic features.

An important consideration of the test results is the correlation between tensile strength and hardness. The correlation is important because it relates directly to the allowable hardness range that is specified in design of components. Figure 35 shows YS and UTS for the steels tested here and other data from Kirby et al. (37) on similar steels plotted against the bulk hardness determined on the Rockwell C scale. The YS predicted for condition D2 in this study from the trend observed for Kirby's data would be less than the measured YS.

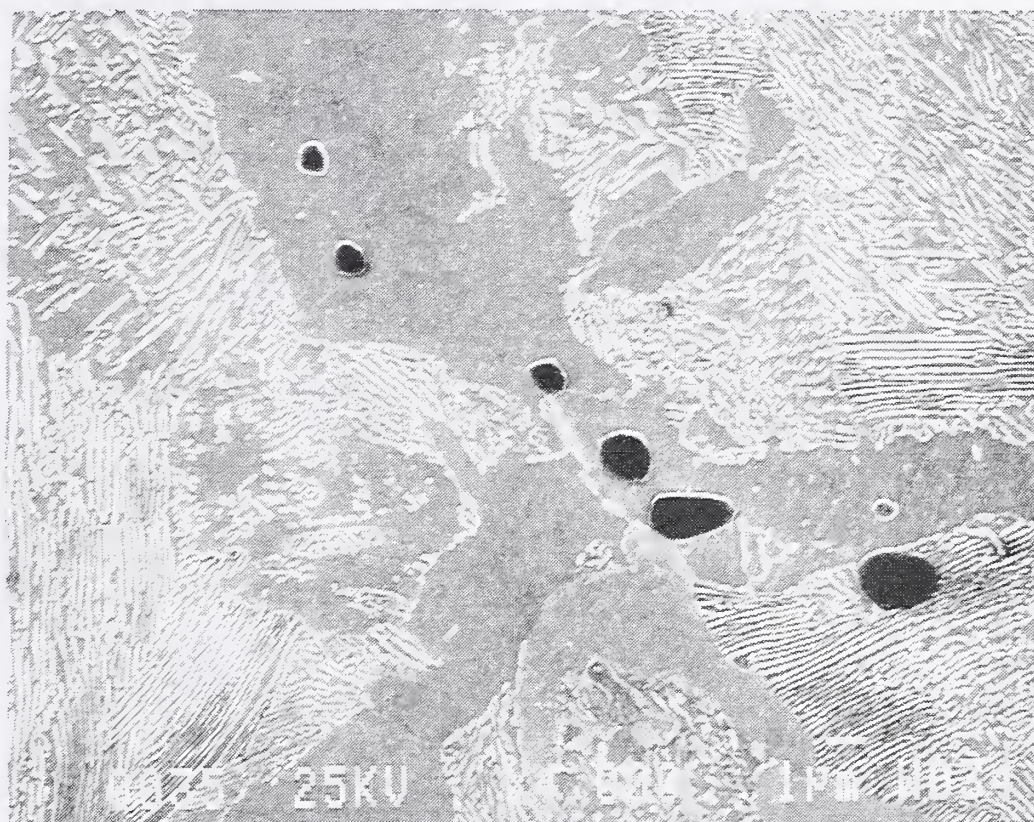


Fig. 34. Microstructure of steel in as-received condition showing the difference in pearlite morphology in different colonies and the MnS inclusions in the  $\alpha$  network.

The evaluation of toughness can be made by comparing the results of tensile fracture properties and the CVN results. The ratio  $\sigma_{rr}$  at fracture/YS is taken as a measure of toughness from the tensile test results. Figure 36 shows a plot of  $\sigma_{rr}/YS$  vs. CVN absorbed energy for the three processing conditions examined in this report and other data on as-rolled bainitic steels whose YS is similar to the SAE 1141-Nb steel (52). The CVN absorbed energy at room temperature for the two types of steels,  $\alpha$ -P and bainitic, are similar, but the toughness in the tensile test is consistently higher for the bainitic steels compared to that of the three deformation conditions evaluated here for SAE 1141-Nb.

The equipment described in this report should produce results that are compatible with the existing, small-scale TMP simulator at NIST. A direct comparison between the results from the two systems can be made for the condition D3 (deformed at 1100°C). The recrystallized prior austenite grain size  $d_{rex}$  after a given true strain  $\epsilon$  can be predicted from the equation shown below:

$$d_{rex} = 0.9 \cdot d_0^{0.67} \cdot \epsilon^{-0.67}, \quad (15)$$

where  $d_0$  is the starting austenite grain size prior to deformation. Predictions from Eq. 15 agree well with the results of the small simulator (46). The measured value for condition D3 from this study, 20  $\mu\text{m}$ , agrees well with that predicted from Eq. 15, 16  $\mu\text{m}$ .

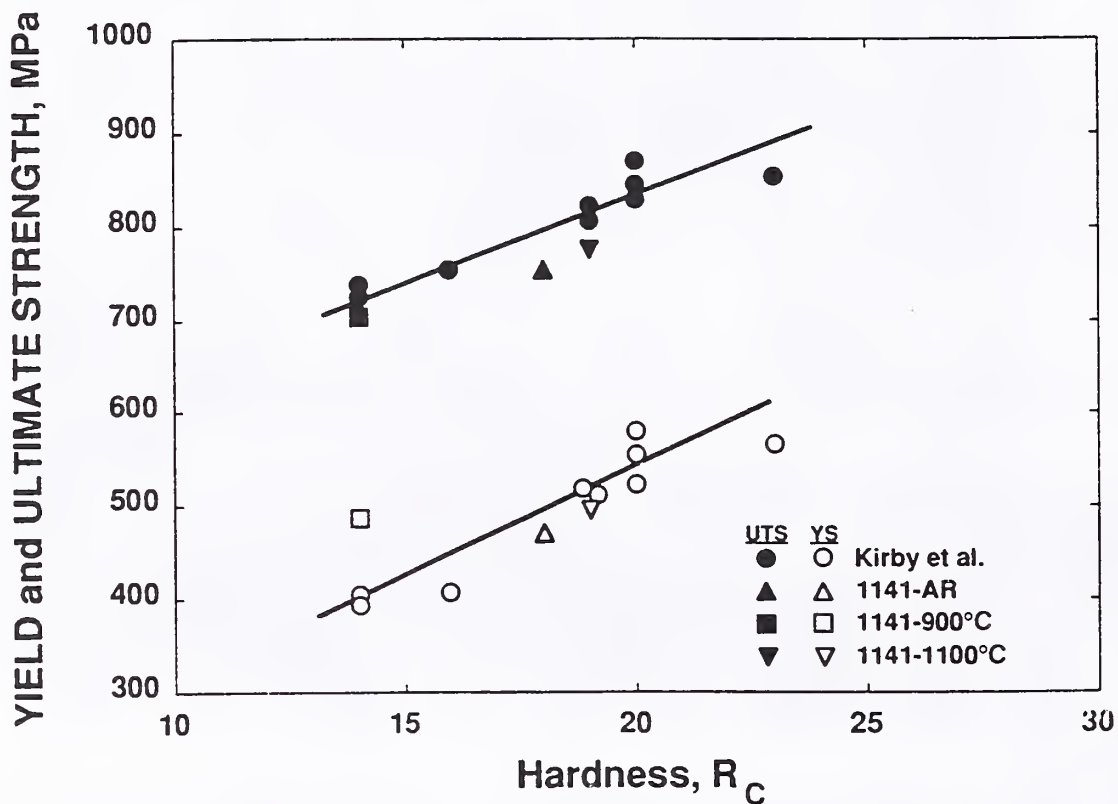


Fig. 35. Plot of strength in uniaxial tension vs. hardness for  $\alpha$ -P steels tested in this study and ref. 36.

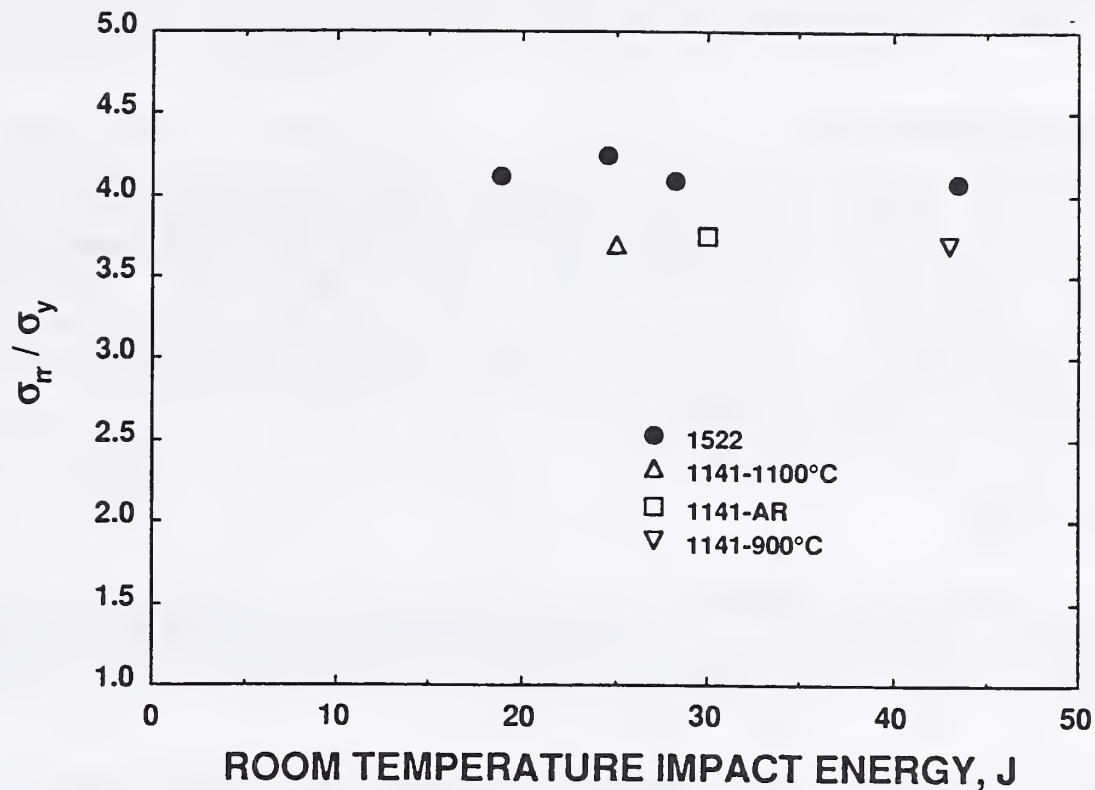


Fig. 36. Plot of tensile test result, ratio between the interfacial stress at fracture  $\sigma_r$  and YS  $\sigma_y$ , and the energy absorbed during CVN testing at room temperature. Data are from this study and ref. 52.

### 3.5 Summary

1. The new, large-scale forging simulator at NIST is capable of producing mechanical test data for the evaluation of the structure-property relationships in steels.
2. Results from the new, large-scale simulator are consistent with those produced on the existing small-scale TMP simulator.
3. Existing correlations between microstructure and properties for  $\alpha$ -P steels can predict YS, UTS, and % RA, but the difference between measured and predicted can be as much as 100 MPa.
4. The evaluation of toughness is a major issue in the application of  $\alpha$ -P steels. Impact testing is not a reliable indication of performance in many important industrial applications where  $\alpha$ -P steels could be used. A major component of our research here at NIST should be directed at the development

of measurement technology for the evaluation of toughness which is consistent with the application (fitness-for-purpose) and future modeling efforts.

#### 4. ACKNOWLEDGEMENTS

The material used in this study was supplied by the Chrysler Corporation. We also want to thank James Hoffmann and Raymond Filar of Chrysler Corporation, John Ham and Prakash Babu of Caterpillar Tractor, William Heitmann of Inland Steel, and Michael Burnett of Timken Corporation for their help and advice in the preparation of this document.

#### 5. REFERENCES

1. J.H. Woodhead, "Review of Principles of Microalloyed Bar and Forging Steels," in Fundamentals of Microalloying Forging Steels, eds. G. Krauss, S.K. Banerji, The Metallurgical Society, Inc., 1987, pp. 3-18.
2. F.B. Pickering, "The Spectrum of Microalloyed High Strength Low Alloy Steels," in HSLA Steels Technology & Applications, ed. by M. Korchynsky, American Society of Metals, Metals Park, OH, 1984, pp. 1-32.
3. M. Korchynsky and J.R. Paules, "Microalloyed Forging Steels - A State of the Art Review," Technical Paper No. 890801, SAE, Warrendale, PA, 1989.
4. J.H. Hoffmann and R.J. Turonek, "High Performance Forged Steel Crankshafts - Cost Reduction Opportunities," Technical Paper No. 920784, SAE, Warrendale, PA, 1992.
5. A.M. Sage, "The Effect of Some Variations in Composition on the Properties of Vanadium Forging Steels," in Fundamentals of Microalloying Forging Steels, eds. G. Krauss, S.K. Banerji, The Metallurgical Society, Inc., 1987, pp. 239-254.
6. S. Engineer, B. Huchtemann, and V. Schuler, "A Review of the Development and Application of Microalloyed Medium-Carbon Steels," in Fundamentals of Microalloying Forging Steels, eds. G. Krauss, S.K. Banerji, The Metallurgical Society, Inc., 1987, pp. 19-38.
7. S. Gunnarson, H. Ravenshorst, and C.-M. Bergstrom, "Experience with Forged Automotive Components in Precipitation Hardened Pearlitic-Ferritic Steels," in Fundamentals of Microalloying Forging Steels, eds. G. Krauss, S.K. Banerji, The Metallurgical Society, Inc., 1987, pp. 325-338.

8. R.S. Cline and J. McClain, "Evaluation of Medium Carbon Microalloyed Steels for Crankshaft Applications," in Fundamentals of Microalloying Forging Steels, eds. G. Krauss, S.K. Banerji, The Metallurgical Society, Inc., 1987, pp. 339-350.
9. P.B. Babu, D.R. Gromer, D.J. Lingenfelter, and G.P. Shandley, "Design for Fracture Resistance in Microalloyed Steel Components," in Fundamentals of Microalloying Forging Steels, eds. G. Krauss, S.K. Banerji, The Metallurgical Society, Inc., 1987, pp. 389-424.
10. A. Rosi, A. Mascanzoni, G. Crispoldi, and F. DeMeo, "Development of a Nb-Ti-N Steel for Production of Tractor Links by Hot Forging and Direct Quenching," in Fundamentals of Microalloying Forging Steels, eds. G. Krauss, S.K. Banerji, The Metallurgical Society, Inc., 1987, pp. 351-366.
11. P. Babu and M.C. Kim, "Ausforging (Direct Quenching) of C-Mn-B Steels," in Fundamentals of Microalloying Forging Steels, eds. G. Krauss, S.K. Banerji, The Metallurgical Society, Inc., 1987, pp. 367-388.
12. P.H. Wright, T.L. Harrington, W.A. Szilva, and T.R. White, "What the Forger Should Know About Microalloy Steels," in Fundamentals of Microalloying Forging Steels, eds. G. Krauss, S.K. Banerji, The Metallurgical Society, Inc., 1987, pp. 541-566.
13. Y. Koyasu, T. Takahashi, N. Ishii, H. Takada, and H. Takeda, "High Strength and Toughness Microalloyed Forging Steels for Fabrication of Automobile Underbody Parts without Subsequent Heat Treatment," Nippon Steel Technical Report No. 47, October 1990, pp. 37-46.
14. K. Grassl, S.W. Thompson, and G. Krauss, "New Options for Steel Selection for Automotive Applications," Technical Paper No. 890508, SAE, Warrendale, PA, 1989.
15. E.A. Petersen, P. York, and S.W. Thompson, "Effects of Microstructure Type on the Notch Toughness of Direct-Cooled Bar and Forging Steels," in MT-ISS-091-008, Annual Report, March 1991 to the Iron and Steel Society Ferrous Metallurgy Grant Program at the Colorado School of Mines, ed. by S.W. Thompson, Colorado School of Mines, Golden CO, 1991, pp. 57-91.
16. Y. Tomota and I. Tamura, "Mechanical Behavior of Steels Consisting of Two Ductile Phases," Transactions ISIJ, Vol. 22, 1982, pp. 665-677.

17. M.H. Poech and H.F. Fischmeister, "Deformation of Two-Phase Materials: A Model Based on Strain Compatibility," *Acta Metallurgica et Materialia*, Vol. 40, 1992, pp. 487-494.
18. T. Gladman and F.B. Pickering, "The Effect of Grain Size on the Mechanical Properties of Ferrous Materials," in Yield, Flow and Fracture of Polycrystals, ed. T.N. Baker, Applied Science Publishers, Ltd., London and New York, 1983, pp. 141-198.
19. T.D. Davies, N.J. Hurd, P.E. Irving, and D. Whittaker, "Fatigue and Machinability Performance of Air Cooled Forging Steels," in Fundamentals of Microalloying Forging Steels, eds. G. Krauss, S.K. Banerji, The Metallurgical Society, Inc., 1987, pp. 435-460.
20. K.A. Taylor and S.S. Hansen, "Effects of Vanadium and Processing Parameters on the Structures and Properties of a Direct-Quenched Low-Carbon Mo-B Steel," *Metallurgical Transactions*, Vol. 22A, 1991, pp. 2359-2374.
21. M. Leap, E.L. Brown, P. Mazzare, and G. Krauss, "The Evolution of Microstructure and Precipitate Dispersions During Reheating in a Vanadium Modified 1045 Steel," in Fundamentals of Microalloying Forging Steels, eds. G. Krauss, S.K. Banerji, The Metallurgical Society, Inc., 1987, pp. 91-112.
22. D. Whittaker, "Micro-alloyed Medium Carbon Steels for Forging," *Metallurgia*, April 1979, pp. 275-281.
23. T. Gladman, B. Holmes, and I.D. McIvor, "Effects of Second-Phase Particles on Strength, Toughness, and Ductility," in Effect of Second-Phase Particles on the Mechanical Properties of Steel, Iron and Steel Institute, London, 1971, pp. 68-78.
24. E. Hornbogen and G. Staniek, "Grain-Size Dependence of the Mechanical Properties of an Age-Hardened Fe-1%Cu Alloy," *Journal of Materials Science*, Vol. 9, 1974, pp. 879-886.
25. Y.-W. Cheng and A. Tomer, "Continuous-Cooling Transformation Characteristics and High-Temperature Flow Behavior of a Microalloyed SAE 1141 Steel," National Institute of Standards and Technology, NISTIR 3964, February 1991, pp. 1-30.
26. A.R. Rosenfield, G.T. Hahn, and J.D. Embury, "Fracture of Steels Containing Pearlite," *Metallurgical Transactions A*, Vol. 3A, 1972, pp. 2797-2804.

27. A.R. Marder and B.L. Bramfitt, "The Effect of Morphology on the Strength of Pearlite," *Metallurgical Transactions A*, Vol. 7A, 1976, pp. 365-372.
28. R. Lagneborg, O. Sandberg, and W. Roberts, "Optimization of Microalloyed Ferrite-Pearlite Forging Steels," in Fundamentals of Microalloying Forging Steels, eds. G. Krauss, S.K. Banerji, The Metallurgical Society, Inc., 1987, pp. 39-54.
29. V. Ollilainen, H. Hurmola, and H. Pontinen, "Mechanical Properties and Machinability of a High-Strength, Medium-Carbon, Microalloyed Steel," *Journal of Materials for Energy Systems*, Vol. 5, No. 4, American Society for Metals, March, 1984, pp. 222-232.
30. W.E. Heitmann and P.B. Babu, "Influence of Bainite in the Microstructure on Tensile and Toughness Properties of Microalloyed Steel Bars and Forgings," in Fundamentals of Microalloying Forging Steels, eds. G. Krauss, S.K. Banerji, The Metallurgical Society, Inc., 1987, pp. 55-72.
31. M.E. Burnett, "Correlation of Forging Parameters to Microstructure and Mechanical Properties in Vanadium Modified 0.40 Percent Carbon Steels," in Fundamentals of Microalloying Forging Steels, eds. G. Krauss, S.K. Banerji, The Metallurgical Society, Inc., 1987, pp. 601-626.
32. K. Onel and J. Nutting, "Structure-Property Relationships in Quenched and Tempered Carbon Steels," *Metal Science*, October 1979, pp. 573-579.
33. J. Heerens and D.T. Read, "Fracture Behavior of a Pressure Vessel Steel in the Ductile-to-Brittle Transition Region," National Institute of Standards and Technology, NISTIR 88-3099, December 1988, pp. 1-39.
34. G.T. Hahn, "The Influence of Microstructure on Brittle Fracture Toughness," *Metallurgical Transactions*, Vol. 15A, The American Society for Metals, June 1984, pp. 947-958.
35. J.F. Knott, "Cleavage Fracture and the Toughness of Structural Steel," in Yield, Flow and Fracture of Polycrystals, ed. T.N. Baker, Applied Science Publishers, Ltd., London and New York, 1983, pp. 81-100.
36. T. Gladman, I.D. McIvor, and F.B. Pickering, "Some Aspects of the Structure-Property Relationships in High-Carbon Ferrite-Pearlite Steels", *Journal of the Iron and Steel Institute*, vol. 210, 1972, pp. 916-930.

37. B.G. Kirby, P. LaGreca, C.J. Van Tyne, D.K. Matlock, and G. Krauss, "Effect of Sulfur on Microstructure and Properties of Medium-Carbon Microalloyed Bar Steels," SAE International Technical Paper Series 920532, Warrendale, PA, 1992, pp. 1-12.
38. T. Ochi, T. Takahashi, and H. Takada, "Improvement of the Toughness of Hot Forged Products Through Intragranular Ferrite Formation," 30th Mechanical Working and Steel Processing Proceedings, Iron and Steel Society, Inc., Lawrence G. Kuhn, publisher, Dearborn, MI, October 1988, pp. 65-72.
39. T.C. Tschanz, G. Krauss and D.K. Matlock, "Short Rod Fracture Toughness Testing of Bar Steels," ASTM STP 1172, to be published by American Society for Testing and Materials, Philadelphia.
40. P.T. Purtscher, J.D. McColskey, and E.S. Drexler, "Aluminum-Lithium Alloys: A Comparison Between ASTM E 813 and E 1304," ASTM STP 1172, to be published by American Society for Testing and Materials, Philadelphia.
41. F.B. Pickering, "Some Aspects of the Relationship Between Microstructure and Mechanical Properties," Iron and Steel, 1965, pp. 110-117.
42. P.T. Purtscher, "Quantifying the Embrittlement Due to Sensitization in an Austenitic Stainless Steel," Scripta Metallurgica et Materialia, Pergamon Press, Vol. 26, 1992, pp. 343-346.
43. F.W. Noble, B.A. Senior, and B.L. Eyre, "The Effect of Phosphorus on the Ductility of 9Cr-1Mo Steels," Acta Metallurgica et Materialia, Vol. 38, No. 5, 1990, pp. 709-717.
44. R.O. Ritchie and R.M. Horn, "Further Considerations on the Inconsistency in Toughness Evaluation of AISI 4340 Steel Austenitized at Increasing Temperature," Metallurgical Transactions A, Vol. 9A, 1978, pp. 331-341.
45. W. Heitmann, Inland Steel Research, 3001 East Columbus Drive, East Chicago, IN, 46312, private communication, March 1992.
46. P. Babu and J. Ham, Caterpillar Tractor Company, Technical Center, Bldg. E, Peoria, IL, 61656-1875, private communication, March 1992.
47. M. Burnett, Timken Company, 1835 Dueber Ave. S.W., Canton, OH, 44706-2798, private communication, March 1992.

48. J.P. Houin, A. Simon, and G. Beck, "Relationship between Structure and Mechanical Properties of Pearlite between 0.2% and 0.8%C," Transactions ISIJ, Vol. 21, Laboratoire de Metallurgie Associe au CNRS, Cedex, France, 1981, pp. 726-731.
49. N. Ridley, M.A. Malik, and G.W. Lorimer, "Partitioning and Pearlite Growth Kinetics in an Ni-Cr Eutectoid Steel," Materials Characterization, Vol. 25, Elsevier Science Publishing Co., Inc., New York, 1990, pp. 125-141.
50. R.M. Kuziak and Y.-W. Cheng, "The High-Temperature, High-Strain Rate Flow Behavior of a Nb-Treated Bar Steel," to be published in proceedings of International Symposium on Processing, Microstructure, and Properties of Microalloyed, and Other Modern High Strength Low Alloy Steels, Pittsburgh, PA, TMS, June 4-6, 1991.
51. Y.-W. Cheng, "Continuous-Cooling-Transformation Diagrams of a Nb-Treated SAE 1141 Steel," to be published in proceedings of International Symposium on Processing, Microstructure, and Properties of Microalloyed, and Other Modern High Strength Low Alloy Steels, Pittsburgh, PA, TMS, June 4-6, 1991.
52. D.A. Shepherd, work in progress, M.S. Thesis, Colorado School of Mines, Golden, CO, 1991.

## APPENDIX A

### Stress Analysis

Argon et al. (A1) found that, for extremes in strain-hardening behavior of a model material, the interfacial stress ( $\sigma_{rr}$ ) at an isolated particle could be approximated as

$$\sigma_{rr} \approx \sigma_o + \sigma_T, \quad (1)$$

where  $\sigma_T$  = the hydrostatic stress at the inclusion and  $\sigma_o$  = the true or equivalent plastic flow stress. The presence of the inclusion raises the local stresses across the interface between particle and matrix over the hydrostatic stress by an amount that approximately equals the average plastic flow stress in the region. Their studies suggest that when  $\sigma_{rr}$  reaches a critical value  $\sigma_c$ , void nucleation occurs.

The approach described above can be applied at any point on the stress-strain curve. Prior to necking,  $\sigma_o$  is equal to  $\sigma_2$ , the measured load divided by the actual cross sectional area. After maximum load is reached, the value of  $\sigma_o$  modifies  $\sigma_2$  to account for the change in stress state in the neck of the tensile specimen as follows (A2)

$$\frac{\sigma_o}{\sigma_2} = \frac{1}{[1+(2R/a)] [\ln(1+a/2R)]}, \quad (2)$$

where  $R$  = the radius of curvature of the neck along the tensile axis of the specimen, and  $a$  = the radius of the minimum cross section of the specimen.

The value of  $\sigma_T$  that develops at the particle is a function of  $\sigma_o$  and reflects the stress concentration due to necking. The ratio  $\sigma_T/\sigma_o$  can be described by (A3)

$$\frac{\sigma_T}{\sigma_o} = 1/3 + \ln(1+a/2R - r^2/2aR). \quad (3)$$

The value of  $r$  is the distance from the center of the diameter to the specific point of interest in the cross section. The term  $r^2/2aR$  in Eq. (3) was introduced to take into account the stress distribution through the cross section. In this case, all calculations were made in the center of the cross section where  $r = 0$  and the hydrostatic stress is a maximum.

## References

- A1. A.S. Argon and J. Im, Metallurgical Transactions A, Vol. 6A, 1975, p. 839.
- A2. G. Dieter, in Mechanical Metallurgy, McGraw-Hill, New York, 1976.
- A3. A.S. Argon, J. Im, and A. Needleman, Metallurgical Transactions A, Vol. 6A, 1975, p. 815.





